

Some observational tests of a minimal galaxy formation model

J. D. Cohn^{1,2*}

¹*Space Sciences Laboratory University of California, Berkeley, CA 94720, USA*

²*Theoretical Astrophysics Center, University of California, Berkeley, CA 94720, USA*

17 November 2021

ABSTRACT

Dark matter simulations can serve as a basis for creating galaxy histories via the galaxy-dark matter connection. Here, one such model by Becker (2015) is implemented with several variations on three different dark matter simulations. Stellar mass and star formation rates are assigned to all simulation subhalos at all times, using subhalo mass gain to determine stellar mass gain. The observational properties of the resulting galaxy distributions are compared to each other and observations for a range of redshifts from 0-2. Although many of the galaxy distributions seem reasonable, there are noticeable differences as simulations, subhalo mass gain definitions, or subhalo mass definitions are altered, suggesting that the model should change as these properties are varied. Agreement with observations may improve by including redshift dependence in the added-by-hand random contribution to star formation rate. There appears to be an excess of faint quiescent galaxies as well (perhaps due in part to differing definitions of quiescence). The ensemble of galaxy formation histories for these models tend to have more scatter around their average histories (for a fixed final stellar mass) than the two more predictive and elaborate semi-analytic models of Guo et al (2013); Henriques et al (2015), and require more basis fluctuations (using PCA) to capture 90% of the scatter around their average histories.

The codes to plot model predictions (in some cases alongside observational data) are publicly available to test other mock catalogues at <https://github.com/jdcphysics/validation/>. Information on how to use these codes is in the appendix.

Key words: Galaxies: evolution, formation, haloes

1 INTRODUCTION

Galaxies are expected to form within the deep potential wells of dark matter halos (White & Rees (1978); Blumenthal et al (1984), for a general introduction see Mo, van den Bosch & White (2010)). This galaxy-dark matter connection suggests that simulations of the histories and spatial distributions of dark matter halos can be used as scaffolding for models of galaxy histories and distributions. Simulating galaxy properties based upon dark matter simulations ranges from from detailed semi-analytic models (see, for example, reviews by Baugh (2006); Benson (2010)) of several galaxy properties at all times, which model and predict many different processes, to models such as the halo model which assign galaxies of a certain kind to dark matter halos at a fixed time by requiring that they match observed clustering and number counts (Seljak (2000); Peacock & Smith (2000); Cooray & Sheth

(2002), also see more recent incarnations such as Hearin et al (2016)) or variants such as conditional luminosity functions (Yang, Mo & van den Bosch 2003)) or abundance matching in luminosity and (proxy for) halo mass (e.g. Vale & Ostriker (2006); Conroy & Wechsler (2009)). The resulting galaxy distributions can then be compared to observations, testing the physical assumptions used in their construction. These methods are also used to construct mock galaxy catalogues (synthetic skies) to aid in designing and analyzing galaxy surveys. More time intensive hydrodynamical simulations, which include and thus fix the baryonic physics and subgrid models for each cosmological run are also being developed, see e.g. Borgani & Kravtsov (2012); Neistein et al (2012) for some comparisons of trade-offs. All of these approaches are currently being developed and extended.

Here, a simple model defined by Becker (2015)¹ is explored. It creates statistical samples of galaxy formation

* E-mail: jcohn@berkeley.edu

¹ Becker (2015) more generally gives a probabilistic framework

2 Observational tests of a minimal model

histories based upon the growth of dark matter subhalos, producing stellar masses and star formation rates for every subhalo in the simulation. (In what follows the terms subhalo and halo will be used interchangeably unless specifically noted.) Much of the physics is encapsulated in an average relation between stellar mass and halo growth found by Behroozi, Wechsler & Conroy (2013a); Behroozi, Wechsler & Conroy (2013b). Behroozi, Wechsler & Conroy (2013a) matched observations of stellar mass functions and star formation rates to average dark matter halo histories at a series of redshifts, and found that

$$\frac{dM^*}{dt} \sim f(M_h, z(t)) \frac{dM_h}{dt}. \quad (1)$$

Each subhalo has stellar mass M^* and subhalo mass M_h (virial mass, in their approach). The star formation efficiency $f(M_h, z(t))$ is a weakly time dependent function of subhalo mass M_h and is publicly available at www.peterbehroozi.com/data.html.

The simple Becker (2015) model uses this relation for average stellar mass gain to assign stellar mass and star formation rates to individual subhalos throughout their histories in a dark matter simulation, once a rule for inheriting stellar mass from progenitor galaxies is added. Becker (2015) suggested one such rule for inheriting stellar mass, as well as the addition of a random component to star formation. (Stellar mass is also lost due to aging.) Galaxy distributions produced by the Becker (2015) model, with his simulation, have a $z = 0$ galaxy stellar mass function close to observations. The $z = 0$ star formation rates are also bimodal, although not agreeing as closely with observations in detail (Becker 2015).

A wealth of galaxy properties follow from having a stellar mass and star formation rate attached to each galaxy throughout its history, in addition to the stellar masses and star formation rates themselves. Colors can be found by integrating a stellar population synthesis model over the star formation rate history. Galaxy positions, velocities and environments are immediate, inherited from the host dark matter simulation. In particular, colors are linked to environment inasmuch as environment affects halo growth. It is thus interesting to examine further properties of this model beyond redshift zero, and how it depends upon different simulations and other properties. The inheritance of stellar mass, the definitions of halo mass and halo mass gain, and the underlying dark matter simulation are all varied here, and compared to observations at redshifts 0 to 2. In addition, properties of the ensemble of resulting galaxy formation histories are compared to those of three other methods, two full blown semi-analytic models and one straw man model.

Several other simple models have also been proposed, predicting an assortment of galaxy properties for redshifts zero and above, for example those by Wang et al (2007); Bouché et al (2010); Cattaneo et al (2011); Mutch, Croton & Poole (2013); Lilly et al (2013); Tacchella, Trenti & Carollo (2013); Birrer et al (2014); Lu et al (2014, 2015). The approach in the Becker (2015) model seems closest to that of Mutch, Croton & Poole (2013), as the stellar masses are

tied to subhalo properties directly (with the gas physics implicit).

The underlying simulations and the construction of the galaxy histories are described in §2. In §3, comparisons are made with several observations at different redshifts. The ensemble of galaxy histories of this simple model are compared via PCA (as in Cohn & Van de Voort (2015)) to some other more predictive models based upon dark matter simulations, in §4. Discussion and conclusions are in §5. The appendix §B gives the formulae in detail for the two stellar mass to halo mass prescriptions which are compared to the models in §3.

Appendix §A describes how to make the plots used in §3 for a single mock galaxy catalogue, using codes at <https://www.github.com/jdcphysics/validation/> (the code `valid_suite.py` in the code subdirectory `vsuite`). To use this code, a list of galaxy stellar masses, star formation rates and subhalo masses are needed as input, which can lie in either a light cone, a fixed time periodic box, or just have some fixed redshift and a random position (if generated analytically). Most of the observational data for these tests are in the redshift range 0 to 1, i.e. overlapping with redshifts at the centers of the currently running dark energy survey (DES, www.darkenergysurvey.org) and the upcoming LSST (www.lsst.org).

2 METHOD FOR MAKING GALAXY HISTORIES

2.1 Dark matter histories

The galaxy histories in Becker (2015) are based upon subhalo histories in a particular dark matter simulation. Three different simulations are considered here, with parameters and other details shown in Table 1, along with the names and properties of the different variations constructed with the simulations. Adding a “2” in front of the names listed in Table 1 refers to the inheritance of the stellar mass from the two most massive progenitors rather than just the most massive progenitor, described in §2.2 below. The simulation used by Becker (2015) is also listed for comparison. All of the simulations were done with periodic boxes, with sides of length $\sim 250h^{-1} \text{Mpc}$. They differ in time resolution, particle number, cosmological parameters, methods for making trees and methods for calculating halo masses.

In more detail, the TreePM dark matter simulation was created with the TREEPM (White 2002) code, in a periodic box of side $256h^{-1} \text{Mpc}$. This simulation is described in more detail in Stark et al (2015). It has 128 outputs between redshift 0 and 10, evenly spaced in $\ln a$, the scale factor. Halos are found using the Friends of friends (FoF) algorithm (Davis et al 1985) with linking length $b = 0.168$. Galaxies inhabit simulation subhalos. A central subhalo is the whole FoF halo and a satellite subhalo is the remnant of an FoF halo which has fallen into a larger FoF halo. Satellites are found and tracked using a 6-dimensional phase space finder (Diemand, Kuhlen & Madau 2006), FoF6d, along with tracking between times and skipped outputs as described in White, Cohn & Smit (2010); Wetzel & White (2010). Satellite subhalo masses are taken to be their infall FoF halo mass, which can increase only if a merger occurs, and a satellite is removed when its FoF6d mass falls below 0.007 of its

for combining simulations and observations to get simulated galaxy properties consistent with the chosen observations.

Name	Sim	particles	Ω_m	$\Omega_b h^2$	σ_8	n	h	M_{halo}	ΔM_h	trees
tree	TreePM	2560 ³	0.3085	0.022	0.83	0.9611	0.6777	M_{fof}	all M	Stark et al (2015)
bolp	Bolshoi-P	2048 ³	0.307	0.022	0.823	0.96	0.678	SAM_M_{vir}	Mmp	Rockstar
bolpmvir								M_{vir}	all M	
bolpmmp								M_{vir}	Mmp	
bol	Bolshoi	2048 ³	0.270	0.023	0.820	0.95	0.70	SAM_M_{vir}	Mmp	Rockstar
bolmvir								M_{vir}	all M	
bolmmp								M_{vir}	Mmp	
orig	Becker (2015)	2048 ³	0.286	0.0235	0.82	0.96	0.70	M_{vir}	Mmp	Rockstar

Table 1. Properties of the three dark matter simulations used here, and the one originally used to implement the Becker (2015) model. They have similar volume ($250 h^{-1}$ Mpc sides for all except TreePM, which has a $256 h^{-1}$ Mpc side) but differ in time and mass resolution, cosmology, tree construction and halo mass definition. The names for the variants will be used below. The bolp and bol variants use SAM_M_{vir} , the instantaneous M_{vir} boxcar smoothed over the current, past and future steps (the sum divided by 3) and then combined with the requirement that a descendant mass is never less than the sum of its progenitors (this mass is provided by Rockstar, described in Behroozi et al (2013); Behroozi, Wechsler & Wu (2013)). Accreted mass is found using Eq. 2, “Mmp”, for SAM_M_{vir} (bol and bolp variants) and instantaneous Rockstar mass M_{vir} (bolpmmp, bolmmp and the original Becker (2015) model). Accreted mass is calculated using Eq. 3 for bolmvir and bolpmvir (with instantaneous virial masses M_{vir}), and tree (with instantaneous M_{fof}). Adding a “2” in front of the name refers to the inheritance of the stellar mass from the two most massive progenitors rather than just the most massive progenitor, described in §2.2 below. The TreePM simulation is described in Stark et al (2015), Bolshoi-P is described in Klypin et al (2016); Rodriguez-Puebla et al (2016), and Bolshoi is described in Klypin, Trujillo-Gomez & Primack (2011). The tree constructions are described in Stark et al (2015) for TreePM and Behroozi et al (2013); Behroozi, Wechsler & Wu (2013) (named Rockstar) for the other runs.

infall mass as in Wetzel & White (2010). Phantom halos (with no progenitor) sometimes appear, presumably these are splashback halos, satellites which travelled out of a larger halo far enough to be recognized as a separate halo, rather than remaining a satellite within the larger halo. Phantoms which appear at the last time step are discarded.

The other two simulations used here are the original Bolshoi simulation (Klypin, Trujillo-Gomez & Primack 2011), and its updated counterpart with Planck Collaboration, Ade et al (2013) cosmological parameters, Bolshoi-P (Klypin et al 2016; Rodriguez-Puebla et al 2016). Both simulations are run with ART. These have higher particle mass and slightly smaller box size ($250 h^{-1}$ Mpc) than the TreePM simulation. The two Bolshoi, Bolshoi-P simulations have finer time resolution at late time (after $z \sim 2$) relative to TREEPM. Bolshoi (Bolshoi-P) has in total 181 (178) steps from redshift ~ 14 (17), spaced in steps of constant a . The spacing for Bolshoi changes from $\Delta a = 0.003$ to twice that at $a < 0.6834$, for Bolshoi-P the spacing changes from 0.0076 for $a > 0.8084$ to 0.005 at earlier times. A few output a values seem to be skipped in the Bolshoi simulation. The Bolshoi cosmology differs from that of TreePM, Bolshoi-P, and slightly from the original Becker (2015) simulation, as can be seen in Table 1. The subhalo trees and mass histories are found using the methods of Behroozi et al (2013); Behroozi, Wechsler & Wu (2013), more detail can be found in those papers. The dark matter halo SAM_M_{vir} masses produced by Behroozi et al (2013); Behroozi, Wechsler & Wu (2013) are the virial halo masses M_{vir} , boxcar smoothed over 3 time steps (along most massive progenitors), with the present step in the middle, and with each central subhalo constrained to have mass at least as large as the sum of its progenitors.²

² See code at <https://bitbucket.org/pbehroozi/consistent-trees/overview> for details.

The original Becker (2015) simulation, to which the model parameters were tuned, is closest to Bolshoi in cosmological parameters. It has 100 time steps equally separated in $\ln a$ between $z = 0$ and $z = 12$, i.e. with time step separation slightly larger than TreePM.

The simulations differ in cosmology, subhalo mass (the non-decreasing and smoothed SAM_M_{vir} vs. the instantaneous M_{fof} or M_{vir} which can increase or decrease at each time step), the definition of satellite masses³, tree construction, and the difference in time step spacing (shorter steps at later times in the Bolshoi, Bolshoi-P simulation relative to the TreePM and Becker (2015) simulations). The chosen method to calculate accreted mass is also given, both are from Becker (2015), and are defined in Eqs. 2 (Mmp) and Eq. 3 (all M) below.

2.2 Creating galaxy stellar mass and star formation rate histories

To get stellar masses and star formation rates at each output time, the simulated dark matter subhalo histories described above are tracked through time. They are assigned stellar mass and star formation rates as described in Becker (2015), except for the inheritance of stellar mass (see below):

- At each output time, the accreted halo mass of a galaxy is taken to be the difference between its halo mass at that step

³ Subhalo mass definitions for the Rockstar trees are explained in detail in Behroozi, Wechsler & Wu (2013): the masses are from an M_{vir} spherical overdensity calculation on the particles identified as subhalo members (using the phase space based friends of friend finder for both the subhalo and its host halo). Properties of the mass gain and loss for satellites using this finder are studied in van den Bosch (2016). The analogous M_{fof} for a satellite subhalo is difficult to define in TreePM; their subhalo masses are set to their infall FoF masses and only increase due to mergers.

4 Observational tests of a minimal model

and the weighted sum of the halo masses of its progenitors at the previous time step.

The weights are motivated by the mass definitions of the simulation. For SAM_{vir} masses, and for the Rockstar M_{vir} masses in some cases (including variants here and in Becker (2015)),⁴ only the subhalo mass of the most massive progenitor (M_{mmp}) is subtracted to get the accreted mass of the final subhalo,

$$\Delta M_h(t) = M_h(t) - M_{\text{mmp}}(t_{\text{prev}}). \quad (2)$$

For the TreePM box, with instantaneous M_{for} masses, and for one pair of runs each for the Bolshoi(-P) runs, with the instantaneous M_{vir} masses, the formula suggested for including all progenitor masses in Becker (2015) is used instead:

all M

$$\Delta M_h(t) = M_h(t) - \frac{M_{\text{mmp}}(t_{\text{prev}})}{\sum M_{\text{not mmp}}(t_{\text{prev}})} M_h(t). \quad (3)$$

If $\Delta M_h(t)$ is negative by the above, it is taken to be zero. In both, t is the present time and t_{prev} is the previous time step output.

- The change in stellar mass in this step has two contributions.

$$\Delta M^* = SFE(M_h, z) \Delta M_h f_b + \Delta M_{*,\text{ran}} \quad (4)$$

One contribution is from the star formation efficiency found by Behroozi, Wechsler & Conroy (2013a) as a function of halo mass, times the change in halo mass times the baryon fraction ($f_b = \Omega_b/\Omega_m$). That is, $f(M_h, z)$ in Eq. 1 is taken to be $SFE(M_h, z) f_b$. In practice, the time step between two simulation outputs is divided up into 250 time steps and the halo mass is assumed to change the same amount between each. The star formation efficiencies are tabulated at <http://www.peterbehroozi.com/data.html> as the file `sfe.dat` in the download tarball `sfh_z0_z8.tar.gz`. The version `release-sfr_z0_z8.052913` is used in this paper.⁵

The second contribution is a random addition to the star formation rate given in Becker (2015), times the time step. The random component to the star formation rate $\dot{M}_{*,\text{ran}}$ is drawn by taking a star formation rate from a lognormal distribution⁶ of mean $\log_{10}(10^{-12} \text{yr}^{-1} M^*)$ and scatter $\epsilon = 0.25$. The increase in stellar mass from this random component is $\Delta M_{*,\text{ran}} = \dot{M}_{*,\text{ran}}(t - t_{\text{prev}})$.

- As implied by Eq. 4, the total star formation rate is the random star formation rate plus the star formation rate due to subhalo mass accretion at the last (small, 1/250th) time step.

⁴ For Becker (2015), this choice was motivated by the details of the construction of the star formation efficiencies, which used the most massive progenitor.

⁵ For halo masses or times outside of the range of these efficiencies, the stellar mass is placed on the $M^*(M_h, z)$ relation from Behroozi, Wechsler & Conroy (2013a). In contrast, Becker (2015) started galaxies at redshift 4 on the stellar mass-halo mass relation.

⁶ As this relation was found in Becker (2015) for time steps which are different from those in the 3 simulations used here, the scatter is likely only approximate for a general simulation.

Without the random component, the galaxies with no subhalo mass gain would have zero star formation rate. The majority of the galaxies with star formation only due to this random contribution to star formation rate become quiescent galaxies below.⁷ One way of viewing the whole construction is that galaxies whose subhalos gain mass are roughly put on the star forming main sequence, with scatter due to scatter in subhalo mass gain history, while those which do not gain subhalo mass are quiescent, with some residual star formation inserted by hand.

- For a halo which has just appeared, the resulting stellar mass is the total stellar mass.
 - For a halo which has at least one progenitor in the simulation, the stellar mass at the current time is the newly formed stellar mass calculated above, plus the stellar mass, after aging (below), of the most massive progenitor or of the two most massive progenitors. Each run uses either one rule or the other for all galaxies and times; tree and 2tree (see Table 1 for properties of the tree model) for instance denote inheriting stellar mass from 1 or 2 of the most massive progenitors, respectively.
- The rule for inheriting stellar mass is the main difference between the Becker (2015) model as implemented here and in the original paper. In Becker (2015), the stellar mass of either the most massive or two most massive progenitors is given to a descendant galaxy depending upon whether there are 2 or more than 2 progenitors. This criterion is time step and resolution dependent, as the number of progenitors tends to grow as the time length between outputs grows, or as smaller halos are resolved. As the time steps vary significantly between simulations considered here, both cases were instead considered separately.
- Aging decreases the stellar mass inherited from the progenitors. The fraction of stellar mass lost by time t since formation time t_f is taken to be (Behroozi, Wechsler & Conroy 2013a; Moster, Naab & White 2013)

$$f_{\text{loss}}(t - t_f) = 0.05 \ln\left(\frac{t - t_f}{1.4 \text{ Myr}} + 1\right). \quad (5)$$

For a given discrete time step, stellar mass loss due to aging is taken to be the average over the interval that stars formed (between t_{f1} and t_{f2}), as in Behroozi, Wechsler & Conroy (2013a), Eq. B1,

$$\bar{f}_{\text{loss}}(t, t_{f1}, t_{f2}) = \frac{1}{|t_{f2} - t_{f1}|} \int_{t_{f1}}^{t_{f2}} f_{\text{loss}}(t - t_f) dt_f \quad (6)$$

Aging can cause net stellar mass loss over time, for instance for galaxies with no subhalo mass gain in a particular time step and a random component $\Delta M_{*,\text{ran}}$ in Eq. 4 which is smaller than stellar mass lost to aging.

Applying this algorithm to the histories of all the subhalos in the simulation attaches to each galaxy (subhalo) a stellar mass and star formation rate, at every output time. As noted earlier, further observable quantities can be derived from these galaxy stellar mass and star formation rate histories. The history of star formation in this prescription could be combined with a stellar population synthesis model (such as Bruzual & Charlot (2003), Maraston (2005) or FSPS (Conroy, Gunn, & White 2009; Conroy, White &

⁷ Thanks to M. Becker for explaining this point.

Gunn 2010; Conroy & Gunn 2010)), dust model and initial mass function to give luminosities in different bands, and other observational properties. Morphological and gas properties are not as directly calculable.⁸ Galaxy positions, velocities, and their relation to the cosmological cosmic web are also automatically available from the dark matter simulation, although they will not be used below.

3 OBSERVATIONAL STATISTICS

Applying the Becker (2015) method as above to a simulation produces a box of galaxies with stellar masses and star formation rates, inhabiting host dark matter subhalos in their cosmological large scale structure environment. The full histories of the galaxies are also available and some of their properties are discussed in §4 below.

Many variations of the model (see Table 1) were constructed. For simplicity, only select examples are shown in the figures, while general trends are discussed in the text. The Bolshoi-P and TreePM runs have cosmological parameters closest to the current best fit measurements, and thus presumably the closest to the observations, so the majority of results shown below are for bolp and tree. Although the Bolshoi run (bol) doesn't use the currently favored cosmological parameters, the star formation efficiencies used in Becker (2015) and here are based upon it, and the cosmological parameters are similar to those used the Becker (2015) simulation of the original model. The bol and bolp differences give some indication of the effect of varying cosmological parameters (however, the simulations also have different time steps). Results from the M_{vir} based models for the two Bolshoi simulations, bolmvir and bolpmvir, are used to isolate effects of replacing the smoothed and constrained $SAM_{M_{\text{vir}}}$ masses with M_{vir} and calculating accreted mass using Eq. 3 instead. Becker (2015) used the Rockstar (Behroozi, Wechsler & Wu 2013) M_{vir} and Eq. 2 to calculate accreted mass; this combination is also used for the bolpmp and bolmmp runs. These cases give similar results to bolmvir and bolpmvir, respectively, aside from slightly larger numbers of low stellar mass galaxies, slightly more star forming galaxies at most stellar masses, and somewhat lower stellar masses for a given halo mass. They will not be discussed further.

Below, the stellar mass-star formation rate ($M^* - SFR$) relations for the simulations and the (related) specific star formation rates are shown, along with the separation between star forming and quiescent galaxies found by Moustakas et al (2013) for PRIMUS. For each sample, this diagram is used to estimate the split between star forming and quiescent populations, and then stellar mass functions are calculated for star forming, quiescent and all galaxies in §3.2, and compared to observations. Last, but not least, the simulated stellar mass to halo mass relations are compared to two relations found from observations by Behroozi, Wechsler &

Conroy (2013a) and Moster, Naab & White (2013). Quantities are shown for (sometimes some subset of) redshifts ~ 0 , 0.57, 0.91 and ~ 2 .

3.1 Stellar mass vs. star formation rate

To start, the stellar mass-star formation rate is shown in Fig. 1, for the TreePM based tree, 2tree models (left, solid and dashed respectively) and the Bolshoi-P based bolp, 2bolp models (right, solid and dashed respectively), for a sample of redshifts. The bol model is similar to bolp and the bolmvir model is similar to tree, in that the latter two (which use instantaneous rather than $SAM_{M_{\text{vir}}}$ mass) have a slightly less smooth boundary between different regions (for example at redshift ~ 2). For all the model implementations, there are two peaks clearly visible. The dashed green line is the separation found by Moustakas et al (2013) for PRIMUS (see their Figure 1). In that case ⁹

$$\log(SFR_{\text{min}}) = -0.49 + 0.65(\log M^* - 10) + 1.07(z - 0.1) \quad (7)$$

The by-eye separation between star forming and quiescent galaxies is shown as a solid blue line. It lies at lower star formation rate, and with a steeper slope, than the dashed green PRIMUS separating line. For the bol and bolmvir models the dividing line also has slope 0.8 (rather than 0.65 as in Eq. 7 above), but shifts instead by $(-0.5, -1.3, -1.5, -2.8)$ at redshifts $\sim (0, 0.6, 0.9, 2)$ (compared to $(-0.8, -1.3, -1.6, -2.5)$ for the models above). The observed separation between star forming and quiescent galaxies moves to higher star formation rates as redshift increases (this is seen also in other observations, e.g. Tasca et al (2015)). This trend to higher star formation rate at higher redshift is weaker in the simulated samples.

Part of the differences may be due to the different stellar mass definitions used (the stellar mass assumptions are given for the the observational dashed separating line (PRIMUS), and the star formation efficiencies from Behroozi, Wechsler & Conroy (2013a) (bwc.comp) in Table 2; a comparison of many different observational star formation rates as a function of M^* is found in Speagle et al (2014)). Another difference is that the center of the quiescent branch is at a fixed position (by hand) at all redshifts in the simulations, while observationally the quiescent branch moves to higher star formation rates at higher redshifts. This fixing of the quiescent branch also pins the star forming/quiescent dividing line to lower star formation rates. Presumably the quiescent branch should evolve in position (and perhaps scatter) with redshift.

Slices of specific star formation rate in different mass bins can also be calculated, these are shown in Fig. 2 for the tree, bolp and bolpmvir models (only the 1 progenitor models are shown here, there is not much difference for the 2 progenitor models). The tree model has the most quiescent galaxies, in part because the tree satellites are almost all quiescent (as their subhalo masses are fixed to their infall subhalo mass unless they merge). The satellites in the bolp and bolpmvir versions can (and do) have subhalo and thus stellar mass gain. The bolpmvir model, with instantaneous

⁸ The model also provides an estimate of the intra cluster light or ICL, studied in detail by Becker (2015). As the ICL is not as well characterized for the higher redshifts which are of most interest here, it is not considered.

⁹ Note the typo in Moustakas et al (2013) Eq. 2 which is corrected in-line in the text directly above.

6 Observational tests of a minimal model

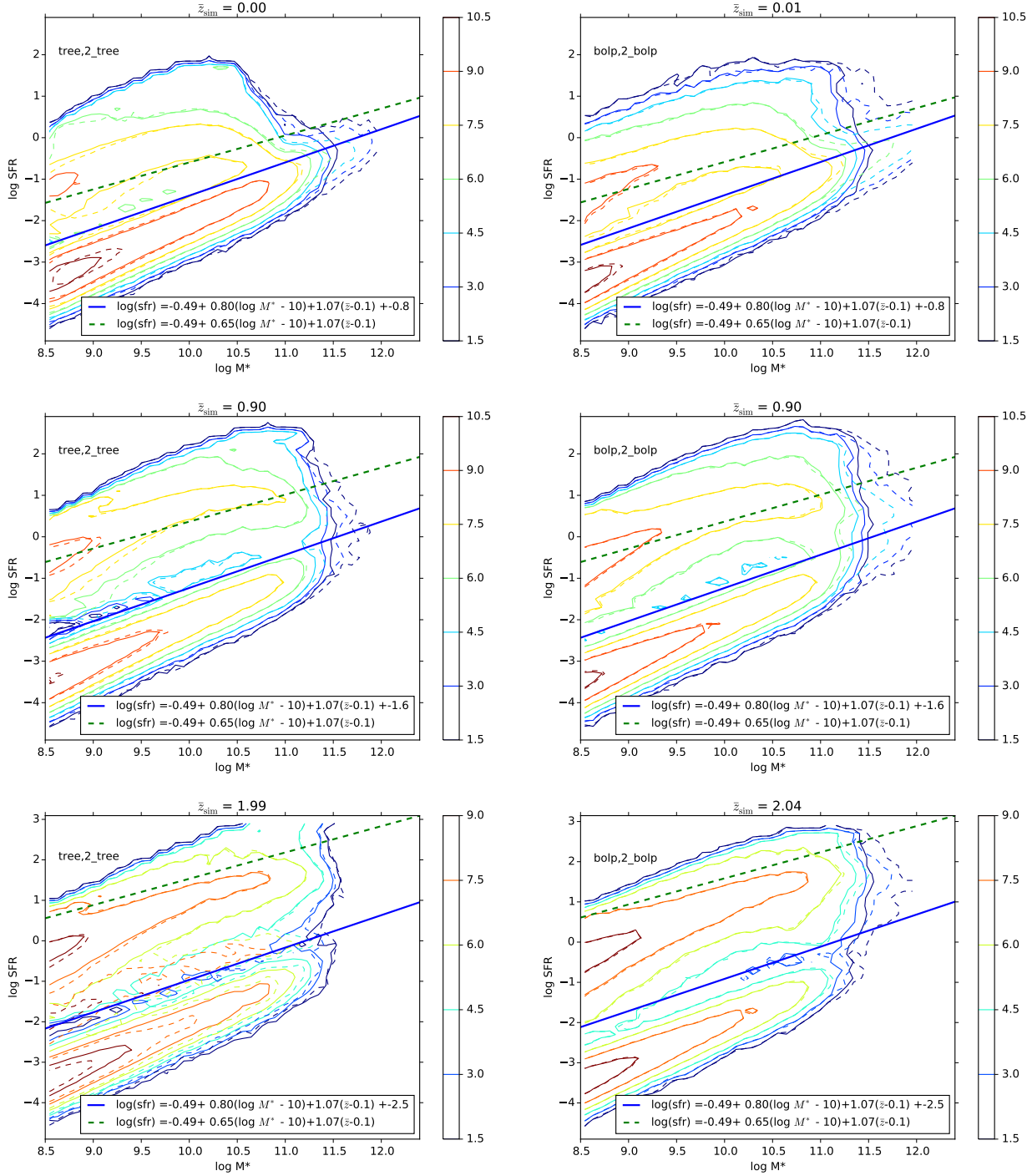


Figure 1. Star formation rate as a function of stellar mass, for 1 progenitor models (solid lines) and 2 progenitor models (dashed lines), for tree, 2tree (left) and bolp, 2bolp (right). The slope and offset for the line separating the models are as listed and were chosen by eye. The dashed line, Eq. 7, is from Moustakas et al (2013) and does not separate the two peaks. The difference between the Moustakas et al (2013) sample and the models may be in part because the former calculate stellar mass using FSPS (Conroy, Gunn, & White 2009; Conroy, White & Gunn 2010; Conroy & Gunn 2010), while the star formation efficiencies for the models constructed here use BC03 (Bruzual & Charlot 2003) stellar masses. Contours are given by arcsinh of galaxy counts in each pixel, to enhance the range shown.

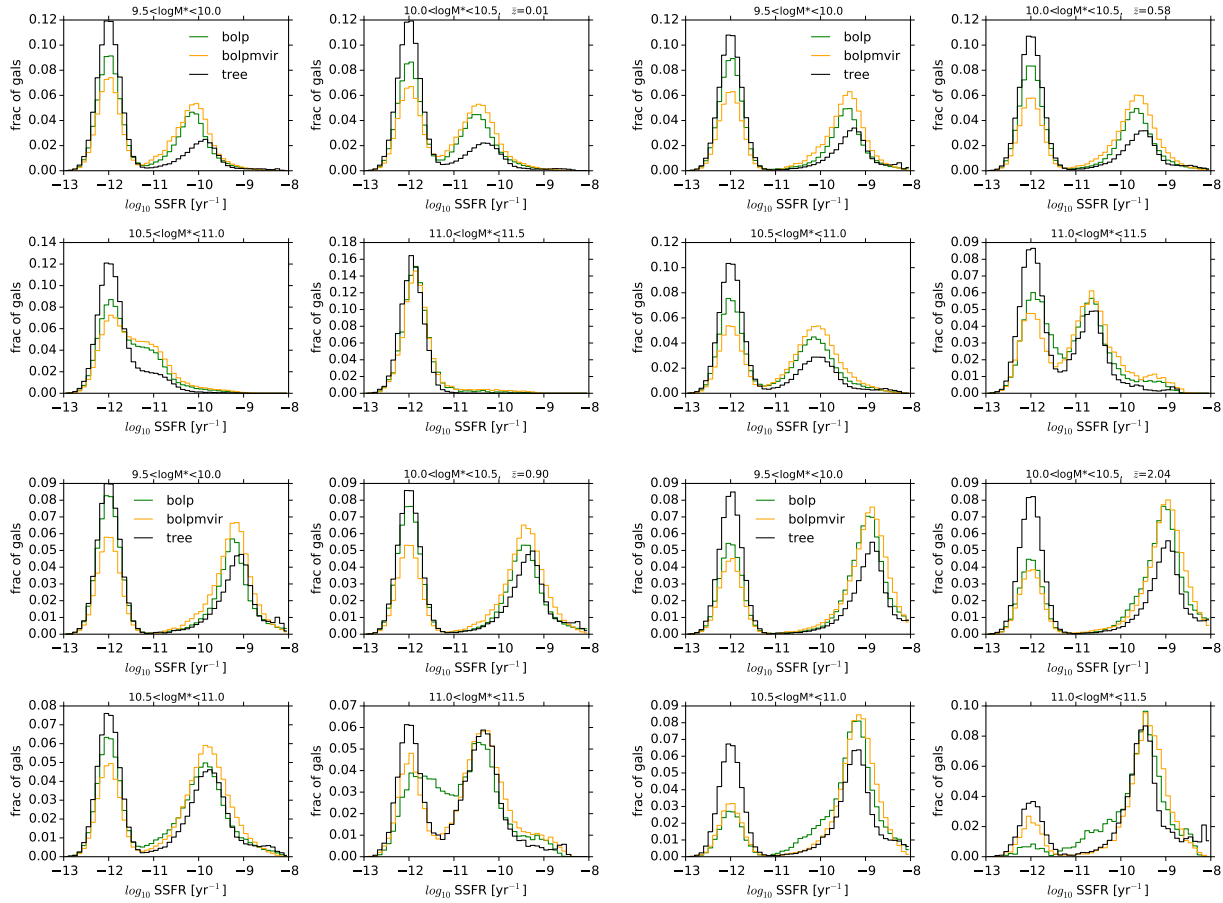


Figure 2. Specific star formation rate in four stellar mass bins (as indicated in each panel) for the tree, bolp and bolpmvir models at redshifts 0.01, 0.58, 0.9 and ~ 2 . The 1 and 2 progenitor models are very similar in specific star formation rates, so only the 1 progenitor models are shown. The left side peak is highest for the tree model, because the tree model satellites, aside from mergers, have only the random star formation term, Eq. 4, as their star formation rate.

mass gain, has more galaxies with high specific star formation rates than the smoothed and constrained $SAM_{M_{\text{vir}}}$ bolp model (also seen for bolpmvir compared to bol). The instantaneous mass M_{vir} is presumably more stochastic in mass gain than its smoothed and constrained counterpart. At the highest stellar masses, the smoothed and constrained bolp specific star formation rates often show a less clean bimodality than the bolpmvir or tree specific star formation rates.

3.2 Stellar mass functions

The relations used to get stellar mass and star formation rates were measured for average binned halo mass and stellar mass gains. The model here uses these rates to assign stellar mass and star formation rates to individual galaxies. As the average of a non-linear function of some quantity is not the same as the non-linear relation on the average of that quantity, the resulting average stellar mass functions and star formation rates may or may not agree with observations. Here, the resulting stellar mass functions are compared to each other and observations for all, quiescent and star forming galaxies.

3.3 Observational stellar mass functions

Before comparing with observations, it should be noted that the available observational stellar mass functions do not all completely overlap, even including their error bars. In Table 2, the different stellar mass function observations used are listed, along with many of their properties. At the bottom are two compilations, from Behroozi, Wechsler & Conroy (2013a) and Henriques et al (2015). Although stellar mass is motivated in part by the wish to reduce differences between observations (such as different wavebands), assumptions made in calculating stellar masses can differ between observations and between the models used to predict the stellar masses. The surveys whose data are shown below were analyzed with a variety of stellar population synthesis models, dust models, initial mass functions (IMF), and cosmological parameters, as listed in Table 2.

The Becker (2015) model for assigning stellar mass and star formation rates has specific choices for these properties built in as well. It uses star formation efficiencies from Behroozi, Wechsler & Conroy (2013a), corresponding to a Bruzual & Charlot (2003)(BC03) stellar population synthesis model, with Blanton & Roweis (2007) dust and a Chabrier IMF (they convert all measurements they use to

8 Observational tests of a minimal model

Name	Reference	z bin edges	area	SPS model	Dust	IMF	Active vs. Quiescent
SDSS-GALEX	Moustakas et al (2013) Table 3	$\bar{z} \sim 0.1$	6956 deg ²	FSPS	Charlot & Fall (2000)	Chabrier	SFR- M^* Eq. 7
PRIMUS_fsp	Moustakas et al (2013) Table 4	(0.2,0.3,0.4, 0.5,0.65,0.8,1.0)	5.5 deg ²	FSPS	Charlot & Fall (2000)	Chabrier	SFR- M^* Eq. 7
PRIMUS_bc03	www.peterbehroozi.com	as above	as above	BC03	Blanton & Roweis (2007)	Chabrier	n/a
ZFOURGE	Tomczak et al (2014) Table 1	(0.2,0.5,0.75,1)	316 arcmin ²	BC03	FAST (Kriek et al 2009) $A_V \in [0,4], Z_\odot$	Chabrier	UVJ
COSMOS/ Ultravista	Muzzin et al (2013) cosmos2.phy.tufts.edu/ ~danilo/Downloads.html	(0.2,0.5,1.0, 1.5,2.0,2.5, 3.0,4.0)	1.6 deg ²	BC03	Calzetti et al (2000)	Kroupa (converted)	UVJ
VIPERS	Moutard et al (2016) Table 2	(0.2,0.5,0.8 1.1,1.5)	>22 deg ²	BC03	Calzetti et al (2000) + 2 other	Chabrier	NUVrK
Compilation	Reference	\bar{z}		SPS model	Dust	IMF	Active vs. Quiescent
bwc_comp	Behroozi, Wechsler & Conroy (2013a) Fig. 3	(0.,0.5,1.,2.)		BC03	Blanton & Roweis (2007)	Chabrier	N/A
Hen15	Henriques et al (2015) http://galformmod.mpa-garching.mpg.de/ public/LGalaxies/figures_and_data.php	(0.1,0.4,1., 2.,3.)		Maraston (2005) (converted)		Chabrier	

Table 2. Observational data sets included. Additional references are Straatman et al (2016) for ZFOURGE and Marchesini et al (2009, 2010) for COSMOS/Ultravista. The conversions used for Kroupa to Chabrier IMF and for Maraston (2005) to BC03 stellar population synthesis are described in the text.

this common basis, i.e. that used by the bwc_comp compilation in Table 2).

For some of the observational data available at these redshifts, the stellar population synthesis models are instead either FSPS (Conroy, Gunn, & White 2009; Conroy, White & Gunn 2010; Conroy & Gunn 2010) or Maraston (2005). Maraston (2005) is used by the Henriques et al (2015); the conversion to BC03 is taken from that paper, i.e. (Dominguez Sanchez et al 2011), $\log_{10} M_{\text{Mar}}^* = \log_{10} M_{\text{BC03}}^* - 0.14$. Conversions between BC03 and FSPS are not available. Dust models also include those by Charlot & Fall (2000); Calzetti et al (2000) and others, and the COSMOS-Ultravista (Muzzin et al 2013) observations use a Kroupa IMF instead of a Chabrier IMF. The stellar mass functions based on the Kroupa IMF are converted by rescaling the Kroupa M^* by 0.61/0.66 (Madau & Dickinson 2014).

In addition to variations in stellar mass definitions, different surveys have different definitions of quiescent and star forming (shown in the last column of Table 2). Moustakas et al (2013) use the SFR- M^* relation in Eq. 7 above, also shown in Fig. 1 as a dashed line in each panel. It is not a good fit for the models here (again because the center of the quiescent branch in the models does not change with redshift, and likely because also PRIMUS uses a different population synthesis model and dust model than that used to calculate the star formation efficiencies in Behroozi, Wechsler & Conroy (2013a)). In more detail, the PRIMUS SFR is calculated via iSEDfit (as is M^*), which takes measurements in all of their specific filters. In contrast, Tomczak et al (2014); Muzzin et al (2013) separate quiescent and active stellar galaxies using UVJ and Moutard et al (2016) separate colors using NUVrK. For comparison with the simulations,

the stellar mass functions for the quiescent and star forming populations are simply plotted as given (after any known conversions for stellar mass or IMF have been included as above). As can be seen below, sometimes, but not always, the UVJ and NUVrK separated stellar mass functions have strong overlap with the stellar mass functions found using the star formation - M^* cut, Eq. 7 of Moustakas et al (2013).

Conversions between these different definitions of stellar mass and quiescence are not always straightforward without reanalyzing the full observational sample, and the data required for conversions are not always available. Comparisons of one fixed observational data set with several different stellar mass modeling assumptions are found in the appendix of Moustakas et al (2013) for PRIMUS; tools for such comparisons such as EZGAL (Mancone & Gonzalez 2012) can also be used.

One additional consideration is that the observed volumes are often still relatively small, although efforts have been made to estimate the sample variance errors (for example, the sample variance estimate in ZFOURGE follows Moster et al (2011)). It is also possible that the covariance of the scatter between different stellar mass bins described in Smith (2012) may need to be included at some point.

3.4 Comparison between observations and the models

The above observational stellar mass functions were compared to the different models constructed here, at a range of redshifts.

A first example is shown in Fig. 3, for the bol, bolmvir, bolp and tree models at $z = 0$, along with observational data

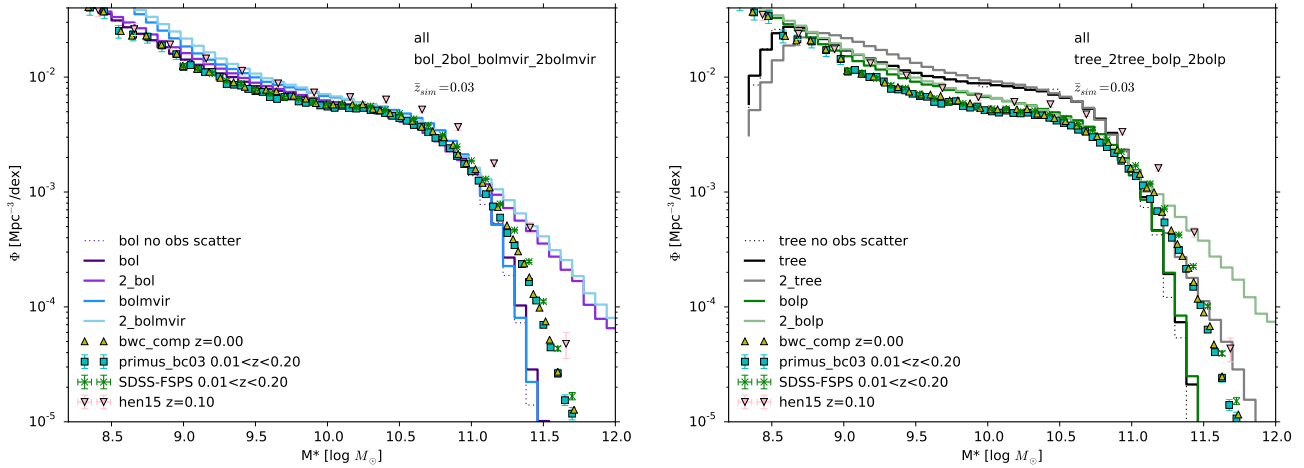


Figure 3. Stellar mass functions for bol and bolmvir models (left) and for tree and bolp models (right), for all galaxies at redshift ~ 0 . Histograms are for the simulations, while points and smooth lines are observations, described in Table 2. The heavier histograms are for the 1 progenitor variants, and all solid histograms include an observational scatter in M^* (see text). The dotted histogram is the data before including scatter, shown for a single model in each panel. The best fit to observations at low stellar mass is for the bol and 2bol models, which coincide with the cosmology and simulation used to calculate the star formation efficiencies implemented in all the models. Changing the cosmology ((2)bolp, at right) increases the stellar mass function at low stellar mass, as does using the instantaneous M_{vir} ((2)bolmvir) or instantaneous M_{fof} ((2) tree, which also has the same cosmology as bolp). At high stellar mass, the observations tend to fall between the 1 and 2 progenitor variants (except for 2tree), implying some combination may work in general.

from Table 2 at the same redshift. The histograms are from the simulations, and include observational scatter via the lognormal ($\log_{10} M^*$) distribution of Behroozi, Wechsler & Conroy (2013a), with variance $\sigma = 0.07 + 0.04z$ as a function of redshift. The dotted histogram shows one of the models (as indicated) without this observational scatter. In this and all figures following, the points and smooth lines are various observational data sets, as indicated and further detailed in Table 2. (The smooth lines are Schechter fits provided as part of the analyses the observations.)

The bol and bolmvir models are based upon the simulations (with a disfavored cosmology) used to calculate the original star formation efficiencies ($SFE(M_h)$ in Eq. 4, by Behroozi, Wechsler & Conroy (2013a)). These may be expected to have the best match to observations as a result. The difference between bol and bolmvir is the choice of mass and method for calculating accreted mass (see Table 1). For both panels at $z = 0$, the models based upon the $SAM_{M_{\text{vir}}}$ smoothed and constrained halos masses give lower stellar mass functions at low stellar mass than the models based upon instantaneous mass (M_{vir} for bolmvir and M_{fof} for tree). The lowest stellar mass function at low stellar mass is for the bol models, which has the best agreement with observations. At high stellar mass, except for the tree variants, the observations fall between the 1 and 2 progenitor models, implying some criteria to mix the two will work (such as the simulation specific criterion of Becker (2015)).

At higher redshift, Fig. 4, the agreement of the bol stellar mass function with observations decreases, while the agreement with observations of the tree stellar mass function varies. The tree model, with instantaneous M_{fof} , tends to be higher than bolp at low redshift, but then falls below it at $z = 0.9$ and closer to the observations. The bolpmvir model, based upon instantaneous M_{vir} and not shown, has stellar

mass functions which are closer than bolp to those of the tree model but with a slightly different shape than the tree model. It is hard to interpret the changes between the tree and bolpmvir model as not only does the average relation between these two mass definitions evolve with redshift, but the details of physical mass gain are likely to differ between these definitions as well.

At $z \sim 2$ the stellar mass functions of the simulated galaxies lie at or slightly above the observations for all models shown, especially near the break in the stellar mass function. The models overlap closely for all models sharing the same cosmology, including those not shown, aside for a small variation at high stellar mass due to 1 or 2 progenitors contributing final stellar mass.

An estimate can be made of the quiescent and star forming stellar mass functions by using the division between the populations in terms of star formation rate and stellar mass seen in §3.1. Again, the caveats about different definitions of quiescent and star forming in the observations should be kept in mind (Table 2). For comparison of star forming and quiescent stellar mass functions, the tree and bolp models will be shown, as they are based upon simulations closer to the current best fit parameters. Their quiescent and star forming stellar mass functions are shown at 4 different redshifts in Fig. 5. In comparison to the observations, the simulated models give too many quiescent galaxies at low stellar mass. For the tree model, some of the quiescent galaxy excess is built in. The tree satellite subhalos only increase their subhalo mass from their infall mass through merging, and so tend to only have the random added by hand component of star formation (in Eq. 4). As a result, the tree model has only small fraction of star forming satellites (about 1 percent). This almost automatic satellite quenching does not occur the Bolshoi and Bolshoi-P based models, which have

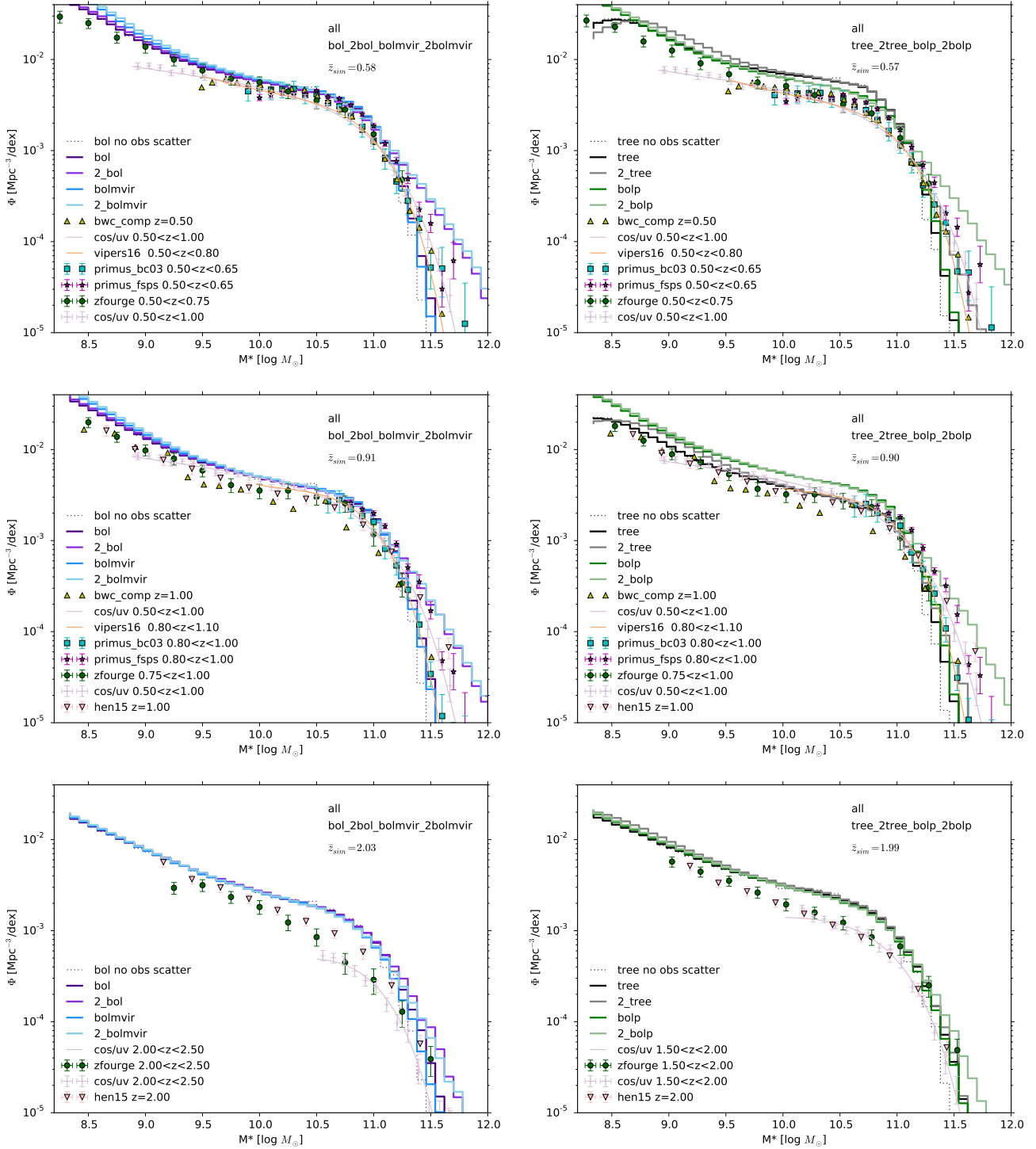


Figure 4. Stellar mass functions for bol and bolmvir models (left), and tree and bolp models (right) for all galaxies at higher redshifts $\sim 0.6, 0.9$ and 2 . Lines and points as in Fig. 3. The agreement of the bol model with observations at redshift ~ 0 diminishes at higher redshifts, rising above the observations at low stellar mass; in contrast the tree model has excellent overlap at $z \sim 0.9$. As redshift increases, the models sharing cosmology but differing in mass definitions and mass gain models become closer. At higher stellar mass the observations tend to lie between the 1 and 2 progenitor models until $z \sim 2$, where all the models tend to overlap, and lie at or slightly above the observations (Table 2).

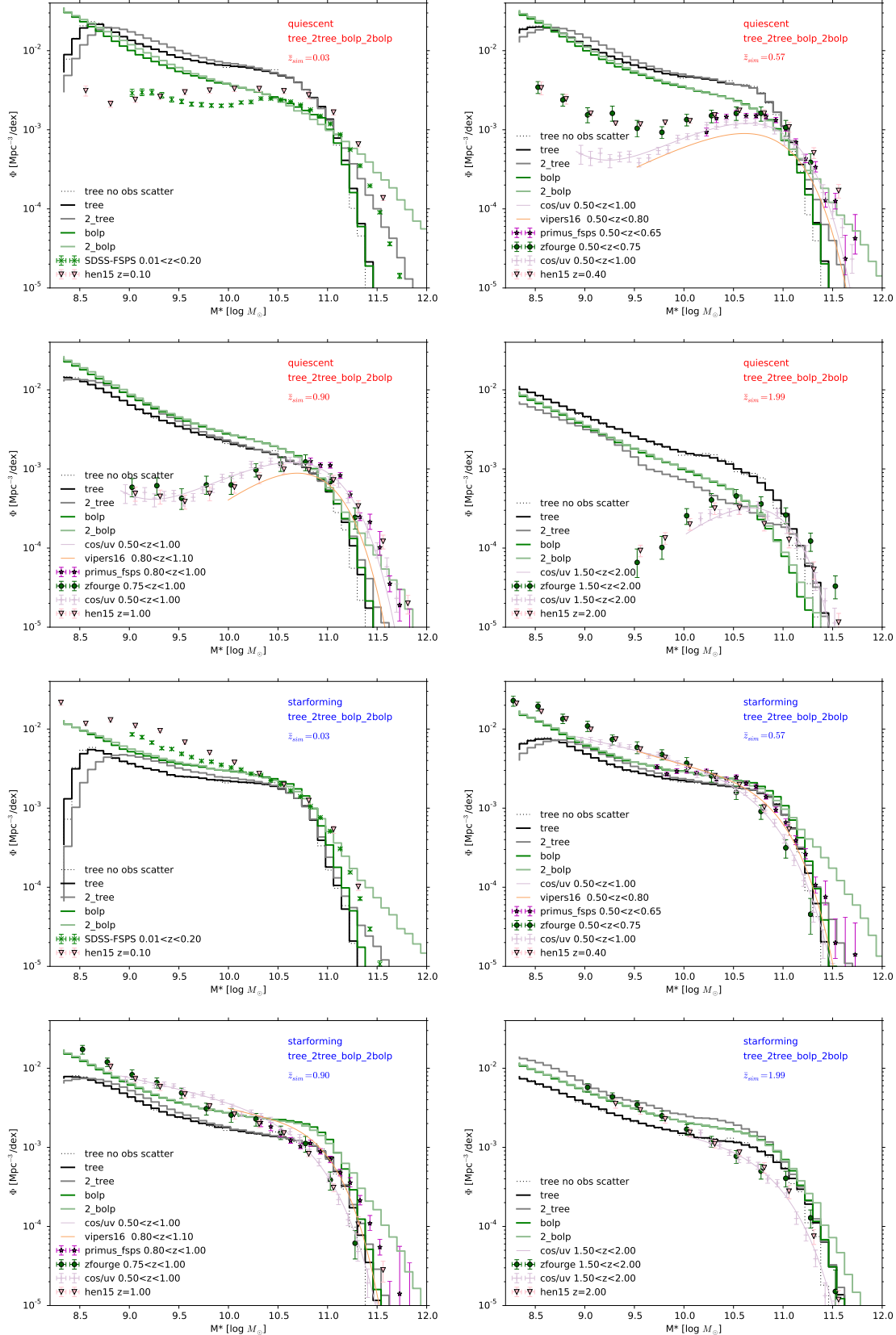


Figure 5. Redshift $\sim 0, 0.6, 0.9, 2$ quiescent stellar mass functions, top, and star forming stellar mass functions, bottom, for tree and bolp. The division between quiescent and star forming is shown in Fig. 1. The observational data are described in Table 2, note different observations have different definitions of starforming and quiescent. The excess of quiescent galaxies for tree results in it having a deficit of star forming galaxies, all models have too many faint quiescent galaxies. Other features as in Fig. 3.

much larger fractions of star forming satellites. However, all of these variants show an excess of quiescent galaxies at low stellar mass (also for the bol, etc., simulations, not shown). This may be made even worse if the center of the quiescent branch (a feature chosen by hand) is moved to a higher specific star formation rate to agree with observations, as suggested by the stellar mass-star formation rate diagrams in §3.1.

To summarize, the model upon which the star formation efficiencies were tuned has a good match to the low stellar mass component of the stellar mass function at $z \sim 0$. For higher stellar mass, the 1 progenitor and 2 progenitor models tend to separate and the observational data usually falls between the two, suggesting the use of some combination of the two models which generalizes the prescription of Becker (2015)) to arbitrary time steps, mass resolution, and perhaps including redshift dependence. There seems to be an excess of low stellar mass quiescent galaxies for all models. At the highest redshift considered, $z \sim 2$, the stellar mass functions of all the models tended to become degenerate, aside from differences due to cosmology, and a small change if 1 or 2 progenitors contributed stellar mass to a galaxy. The models lie mostly above the observed stellar mass function at $z \sim 2$.

3.5 Stellar mass to halo mass relation

A third comparison quantity between the models and observations is how a galaxy of a given stellar mass inhabits a dark matter halo, $M^*(M_h)$. For the simulation based models, this relationship is immediately available.

In Fig. 6, the curves show two measurements of $M^*(M_h)$ from observations, by Moster, Naab & White (2013) and Behroozi, Wechsler & Conroy (2013a). (The functional forms of the curves are in Appendix §B.) As the simulated halo masses are M_{vir} halo masses, and Moster, Naab & White (2013) uses M_{200c} masses, the Moster, Naab & White (2013) curve is shown both with and without an applied average conversion (White 2001) to the halo masses, to give an idea of the size of the conversion effect. These $M^*(M_h)$ fits differ in the assumed cosmology and also in the observations used to derive them. Both use Perez-Gonzalez et al (2008), while Moster, Naab & White (2013) also uses Santini et al (2012), and Behroozi, Wechsler & Conroy (2013a) also use Moustakas et al (2013) in the redshift range 0 – 1. The observational stellar mass functions for both fits have the Bruzual & Charlot (2003) stellar population synthesis models with a Chabrier IMF, and so are expected to be comparable to the Becker (2015) models here, which has both of these assumptions incorporated into the star formation efficiencies. However, the dust model of Moster, Naab & White (2013) might differ. Although the two theoretical curves look different, errors for Behroozi, Wechsler & Conroy (2013a), given in, e.g., the downloads `sfh_z0_z8.tar.gz` available at www.peterbehroozi.com, are often large enough to encompass the average $M^*(M_h)$ for Moster, Naab & White (2013).

The Behroozi, Wechsler & Conroy (2013a) and Moster, Naab & White (2013) curves are compared to the bol, bolmvir, tree and bolp simulated 1 and 2 progenitor models in Fig. 6, at redshift 0 and 2. For simplicity, only the 1 progenitor bol or tree model is shown in detail. In this case, the line in the center of every box is the median, and the

boxes go from lower to upper quartile of the data. The solid black lines above and below are 10th to 90 percentile. For the other 3 models, only the median values are shown: triangles are for the 2 progenitor tree or bolp models, 'X's' for the 1 progenitor bolp and bolmvir models and stars for the corresponding 2 progenitor models. The example shown in detail shows that the median tends to lie near the average of the distribution except towards high halo mass. All galaxies are included here, not just central galaxies. As there is large scatter in the measured $M^*(M_h)$, roughly a factor of two for BWC13 for example (not shown for clarity), the lack of exact agreement with the medians of the distributions in the simulations is not a concern, although all of the model distributions look high at redshift ~ 2 . However, the 2 progenitor models at high stellar mass seem to put galaxies in halos with not enough mass (except for the 2tree model at high redshift). Again, this suggests that a combination of 1 and 2 progenitor models may agree with observations.

To summarize the comparison between the models and observations, the simulated galaxies have stellar mass-star formation rate relations which are clearly bimodal, but which seem to have star formation rates which are low, on the whole, compared to Moustakas et al (2013), and the difference increases with redshift. This may be in part due to difference in stellar mass definitions and the by-hand choice of the position and scatter of the quiescent branch. The models based upon instantaneous halo mass (tree, bolmvir, and bolpvmir) tend to have more features in their stellar mass-star formation rate diagrams, relative to those built upon the smoothed and constrained SAM_{Mvir} . In the specific star formation rate, the models are similar, although the smoothed SAM_{Mvir} models sometimes do not have as clear a break in specific star formation rate between the star forming and quiescent galaxies. The tree models have the largest number of quiescent galaxies, in part because almost all of the satellites are quiescent.

The observed stellar mass function at low redshift agrees best with the simulation which was also used to find the star formation efficiencies as a function of mass (upon which the model here is based). At high redshift $z \sim 2$, all of the simulations have stellar mass functions which overlap, for variants which have the same cosmology (aside from some variation at high stellar mass between to 1 or 2 progenitor versions), and all have some overlap with observations, although the simulations are high near the bend in the stellar mass function. There seems to be an excess of faint quiescent galaxies at all redshifts in all models. The stellar mass to halo mass relations are mostly reasonable, although they tend to be higher than the central values found observationally (albeit based on a now disfavored cosmology), and the 2 progenitor models are far from observational constraints, especially at high halo mass and low redshift. It seems some combination of 1 and 2 progenitor models, with the criteria flexible enough for different time steps and halo mass resolution, may be able to reach the observational values falling in between the two variants for the stellar mass to halo mass relation. Another possibility is to lower the stellar mass per halo via more stellar loss mass into the ICL, even from just one progenitor.

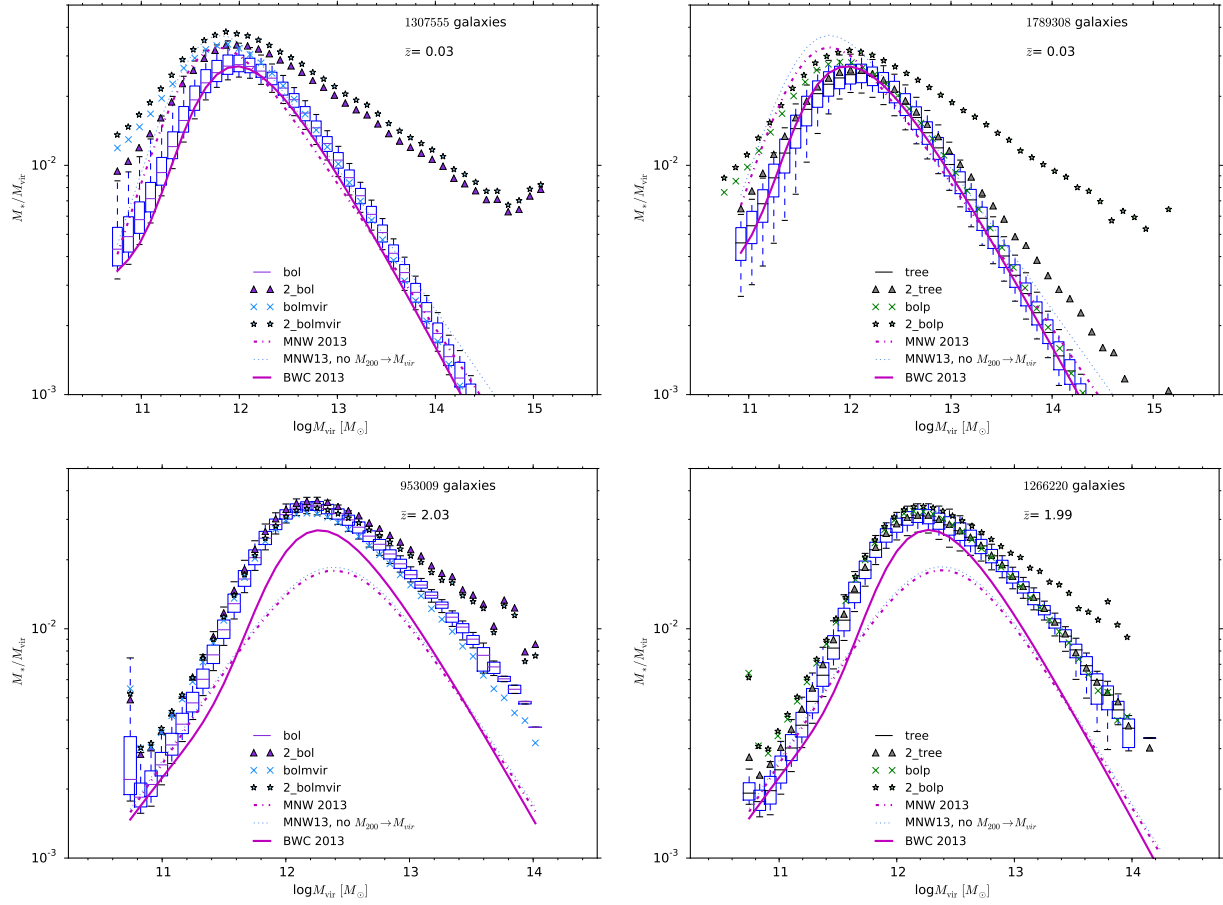


Figure 6. $M^*(M_h)/M_h$ as a function of halo mass M_h for low redshift (top) and high redshift ($z \sim 2$, bottom), for the bol, bolmvir models at left and the tree, bolp models at right. The number of galaxies listed are for the 2bolmvir and 2bolp models, respectively. The two lines for Moster, Naab & White (2013) correspond to the formula directly in their paper (dotted) and converted to M_{vir} (dot-dashed) and the solid line is from Behroozi, Wechsler & Conroy (2013a). The scatter in the measured ratios (not shown) is in the range 30%-50% for most values of M_{vir} . The boxes are for the 1 progenitor bol or tree models, showing upper and lower quartiles around the median value, shown by a line, and the “whiskers” are at 10 and 90 percentiles. For clarity, only the median value for the 2 progenitor bol and tree (triangles) models, the 1 progenitor (X’s) and 2 progenitor (stars) bol and bolmvir models are shown. Galaxies with $M^* < 10^8 M_\odot$ were not included; the low M^* cutoff can introduce spikes at low M_{vir} .

4 ENSEMBLE OF GALAXY FORMATION HISTORIES

The models constructed here are very simple when compared to many others found in the literature and yet seem to have reasonable observational properties. It is thus interesting to see how they compare to semi-analytic models, which use and evolve many more physical halo and galaxy properties, and give many more predictions. One way to compare different galaxy formation models is to look at the ensemble of histories of galaxies they produce. Properties of the histories of galaxy formation, for a large number of galaxies in a model, is another way to characterize how galaxies form in that model. (Individual galaxies can only be followed in detail only in simulations.¹⁰)

In this section the full ensemble of galaxy histories for

several variants of the Becker (2015) model are compared in terms of their average histories, the variance around the average history, the leading fluctuations around the average history and the fraction of variance in several of the (leading) fluctuations around the average history. These quantities are readily available using principal component analysis (PCA). Using PCA, the ensembles of histories of stellar masses, in both a semi-analytic model and a hydrodynamical model, were found to be well approximated as combinations of only a few basis fluctuations around the average history in Cohn & Van de Voort (2015). In this section, histories of the simple models constructed above are compared to histories of the Guo et al (2013); Henriques et al (2015) semi-analytic models built upon the Millennium (Springel, et al 2005; Lemson et al 2006) simulation, which have many more parameters and detailed predictions, and to a straw man model based solely upon subhalo mass.

To implement PCA, the stellar mass history of every galaxy in a simulation is taken to be a vector, with the stellar mass at each time corresponding to a different com-

¹⁰ Methods to deduce histories with increasing detail from observational spectra are also being developed, see, e.g., Pacifici et al (2013, 2016).

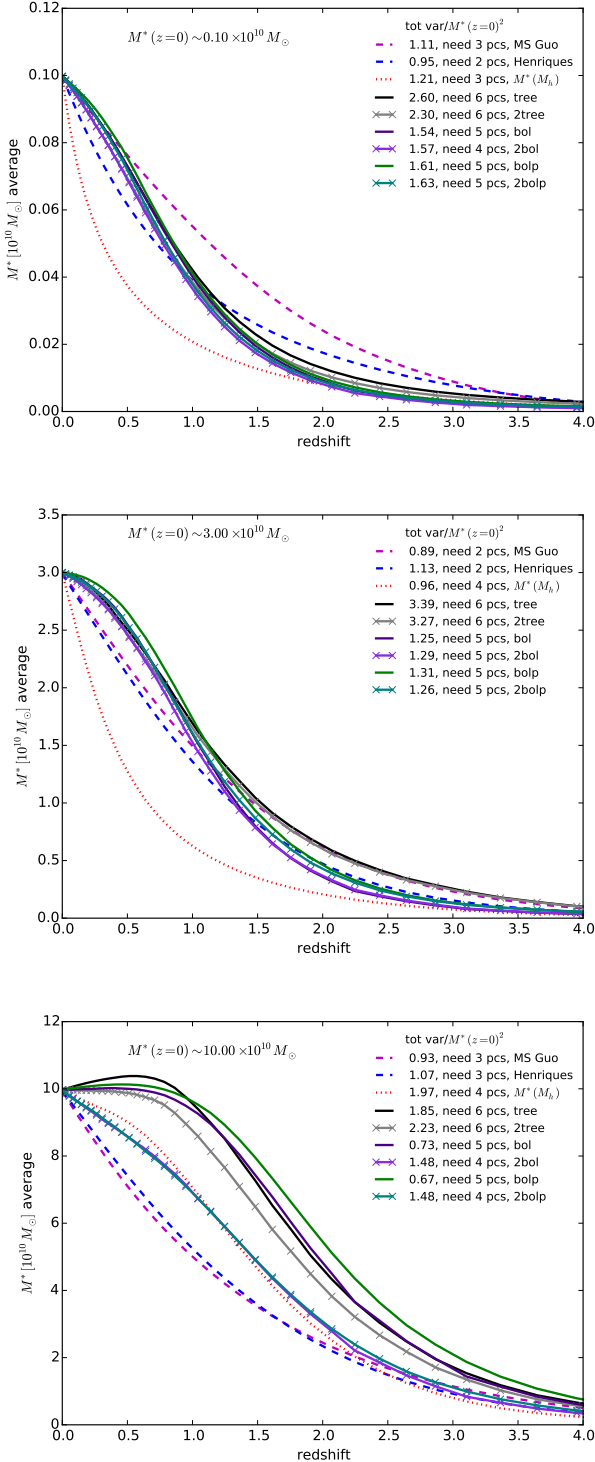


Figure 7. Comparison of average stellar mass histories for 9 different models built on dark matter merger tree histories, for galaxies which have $M^*(z=0) = 10^9, 3 \times 10^{10}$ and $10^{11} M_\odot$, top to bottom. The models are described in the text. The basis fluctuation contributing the largest variance for each of the models tends to peak at earlier times for average histories with earlier stellar mass gain, and to be similar for models with average histories which are similar. The legend shows the normalized total variance/ $M^*(z=0)^2$, and number of principal components (out of 38) needed to get 90 percent of the variance.

ponent of the vector. One can then study and classify the properties of the distribution of these vectors for a given set of histories, i.e. instance of a galaxy formation model. Principal component analysis (PCA), mixture models and k-means clustering were all considered in Cohn & Van de Voort (2015). Here PCA is used, as it gives several quantities to compare besides the separation of histories into classes. PCA is applied by finding the covariance matrix of the different components of the vector of stellar mass histories and diagonalizing it. In Cohn & Van de Voort (2015), the model histories studied from Guo et al (2013) and Schaye et al (2010) had fluctuations around the average stellar mass history which could be described in large part by only 3 basis fluctuations times some coefficients. (In more detail, galaxies compared were taken to have approximately the same final stellar mass, and $\sim 90\%$ or more of the variance around the average was captured by 3 basis fluctuations out of 42). The PCA approach thus compactly describes the full ensemble of stellar mass histories in a model, for any given final stellar mass.¹¹

One of the models from Cohn & Van de Voort (2015) is considered here, for comparison, the Guo et al (2013) model built upon the Millennium (Springel, et al 2005; Lemson et al 2006) simulation. A second updated model, Henriques et al (2015), also built on the Millennium simulation, is used to illustrate the variations found for this method between reasonable semi-analytic models. Along with these, the 1 and 2 progenitor varieties of the tree, bolp and bol models are analyzed using PCA. (As a reminder, galaxies in both 1 and 2 progenitor variants of the Becker (2015) model gain stellar mass from star formation based on their accreted halo mass, however, for the 1 progenitor variant, only the stellar mass of the most massive progenitor is inherited by a galaxy, while in the 2 progenitor variant the stellar mass of the two most massive progenitors is inherited.) In addition, a straw man model is considered, where stellar mass is completely determined by $M^*(M_h, z)$ of Moster, Naab & White (2013). That is, every (sub)halo in the TreePM simulated trees is required to lie exactly on the average $M^*(M_h)$ relation at every time step (although the relation came from abundance matching, this is not abundance matching per se, as scatter is not included). For this straw man model, satellites are assigned $M^*(M_h, z)$ at infall redshift z , and have fixed stellar mass afterwards. The Moster, Naab & White (2013) $M^*(M_h)$ relation is given by Eq. B1 in the appendix, and shown in Fig. 6 for a few redshifts. As this relation requires M_{200c} masses, the FoF masses are converted via White (2001). (This $M^*(M_h)$ model is related to one presented in Moster, Naab & White (2013), which there included scatter.)

As in Cohn & Van de Voort (2015), the histories are studied for small ranges of final stellar masses. In that study, a qualitative change in the history properties occurred around final stellar mass $M^* \sim 3 \times 10^{10} M_\odot$. Thus, here $\sim 10^9 M_\odot$, $\sim 3 \times 10^{10} M_\odot$, and $\sim 10^{11} M_\odot$ are chosen as final stellar masses.¹²

¹¹ Histories of star formation rates require more basis histories, often close to half of the total number of histories, to span the same fraction of their variance. Histories of dark matter halo masses were studied in Wong and Taylor (2011).

¹² More precisely, the range was roughly $9.5\text{--}10.5 \times 10^9 M_\odot$, $2.95\text{--}3.05 \times 10^{10} M_\odot$ and $9.5\text{--}10.5 \times 10^{10} M_\odot$ in final stellar masses. Al-

The different underlying dark matter simulations have different numbers of time steps. The histories are followed from redshift ~ 4.5 to ~ 0 , which takes 42 steps in the Millennium simulation, 38 in the Millennium Planck simulation, 91 in the TreePM simulation, 165 in the Bolshoi simulation and 142 in the Bolshoi-P simulation. Doing PCA on the different histories as given, with their different time steps and numbers of time steps relative to Millennium, leads to much larger scatter in the models explored in this paper, which all have many more time steps than the Millennium simulation. These model histories are thus interpolated to the 38 values where the Millennium Planck based model has outputs, to make the scatter in the histories more directly comparable. (This increase of scatter with number of steps was not as evident when comparing the hydrodynamic simulations, with 20 time steps, with the Guo et al (2013) stellar mass histories, with 42 time steps, in Cohn & Van de Voort (2015).) Other properties, such as the shape of the leading fluctuations, or the number of fluctuations, did not seem to change as much as the number of steps was changed. These interpolated histories with 38 time steps are the ones compared in the figures. In addition, histories where any step had more than a 30% stellar mass drop were taken out, which varied from up to 1 percent in the 2bolp model to 0 in the semi-analytic models.

Some results of PCA analysis of these stellar mass ranges for these nine models are shown in Fig. 7. Each figure (corresponding to a different final stellar mass) shows the average histories for galaxies in each of the 9 models, from redshift 0 to 4.3. The number of PC_n (basis fluctuations around the average) needed to get 90 percent of the variance is shown in the legend, more PC_n (or in a few cases the same) are needed for the simple models explored in this note, relative to the semi-analytic models. This number of components should be compared to the total number of PC_n fluctuation components, 38, to estimate how well a few fluctuations capture the variance of the ensemble of galaxy histories. (Or 37 components, as one component is trivial because the final stellar masses in each set of galaxy histories are all rescaled to coincide before applying PCA.) The larger the fraction of variance due to the first few PC_n , the better the histories can be approximated by only these first few PC_n times some coefficient, added to the average history. The total variance for each model is listed in the legend at right, in units of the final stellar mass squared. The average history and form of the leading fluctuation, PC_0 , are similar using either the original simulation time steps or the interpolated ones. Generally PC_0 (not shown, the fluctuation whose coefficients have the most variance around the average history) has a single peak which tends to be at earlier times for average histories which have earlier stellar mass gain. The results for each different final stellar mass are as follows.

For the lowest final stellar mass example, $M^*(z=0) = 10^9 M_\odot$, the average histories for the Guo et al (2013) and Henriques et al (2015) models differ noticeably from each other. This is consistent with the fact that Henriques et al (2015) models were in part designed to have later formation

of low final stellar mass galaxies than the Guo et al (2013) model. The $M^*(M_h)$ model has even later stellar mass gain. The 6 variants of the Becker (2015) models, independent of cosmology, number of progenitors, or mass definition used, roughly collapse onto one trajectory, with average stellar mass gain later than both semi-analytic models. They do not just track halo mass, although they overlap with the $M^* = M^*(M_h)$ model at early times. Around redshift ~ 2 , they gain stellar mass more quickly than the $M^*(M_h)$ model on average. The leading fluctuation PC_0 around the average galaxy histories is very similar for the 6 models constructed here, and differs for the other 3.

Going to the second plot, for $M^*(z=0) = 3 \times 10^{10} M_\odot$, the two Millennium models become much closer to each other, while the 6 models constructed here start to split into roughly two groups, tree and bol, bolp. At early times, the average tree history is similar to the average Henriques et al (2015) history, however, at redshift 1.5 and after, the stellar mass gain for the tree models increases sharply to join that of the other models constructed here, much more quickly than the two semi-analytic models or the $M^*(M_h)$ model. Not only do the average histories and leading fluctuations split between tree and bol, bolp, but the variance around the two tree models is over twice that for the other four Becker (2015) based models. All 6 models constructed here again require more principal components to capture at least 90% of the variance around the average history, relative to the semi-analytic models. Again, the 1 and 2 progenitor variants have very similar average histories and scatter.

For the highest final stellar mass sample, $M^*(z=0) = 10^{11} M_\odot$, analyzed in the third set of plots, the $M^*(M_h)$ model now has earlier stellar mass gain on average compared to the Millennium based Guo et al (2013); Henriques et al (2015) models, which are similar to each other. (This similarity is expected as much of the change between the two semi-analytic models was aimed at galaxies with lower final stellar mass.) There are significant differences between many of the 6 models constructed using Becker (2015). The average histories for the 2 progenitor bol and bolp models are very close to that of the $M^*(M_h)$ model, while the other variants gain stellar mass much earlier. As these high stellar mass galaxies are often quiescent at late times, it is possible that in the semi-analytic models these high stellar mass galaxies are inheriting stellar mass from even more than two progenitors to get the later stellar mass gain. For this larger final stellar mass, the total variance is higher for the 2 progenitor bol, bolp models and lower for the 1 progenitor bol, bolp models, relative to the semi-analytic models, while both tree variants have more variance around the average history. All six require more PC_n to capture 90% of the fluctuations than the 3 required for both the Guo et al (2013) and Henriques et al (2015) semi-analytic models.

In summary, the average stellar mass histories and fluctuations for the models constructed here differ from those in the two Millennium based semi-analytic models, and the $M^*(M_h)$ straw man model, for all final stellar mass ranges considered. This is independent of dark matter simulation or mass definition used, or how many progenitors contribute to the stellar mass of a descendant halo. However, the models do all have the same star formation efficiency, so other model changes are in principle possible. For low final stellar mass, the different models constructed here have almost the same

average history, and the perturbation of each corresponding to the direction of largest variance is also very similar. As the final stellar mass increased, these models separated out. When they differed, the 1 progenitor models tended to have earlier stellar mass gain than the 2 progenitor models, for fixed final stellar mass.

It is interesting that although the models are simpler in construction than the semi-analytic models, they tend to require more basis fluctuations to capture most of their variance, and their variance around the average history, except for the 1 progenitor models for the largest final stellar mass, is also larger. This might hint at some smoothness in the semi-analytic models that is not captured with the simplifications used here. (For the tree model, some of the variance for the tree model is due to the random star formation. Setting the random star formation to zero for $M^*(z=0) = 3 \times 10^{10} M_\odot$ reduces the variance from by about 20%, however the number of principal components to capture 90% of the variance is unchanged.¹³)

5 DISCUSSION AND CONCLUSIONS

The Becker (2015) model assigns stellar masses and star formation rates to subhalos in a dark matter simulation, primarily using halo mass gain to determine stellar mass gain. Galaxy distributions and histories were calculated for three different dark matter simulations, with differing cosmologies, mass definitions, mass history constructions and time step separations, to find out how much these simulation and other differences affect observable properties in this model, and how well the different variations match current observations at several redshifts.

Bimodality in the star formation rate occurred for all implementations, with the scatter in the star forming branch roughly due to changes in accretion history, and the center and scatter for the quiescent branch put in by hand (which would otherwise be at zero star formation rate). The division between quiescent and star forming galaxies as a function of stellar mass and star formation rate differs from that found in Moustakas et al (2013), but some difference may be due to differences stellar mass definitions. Another difference between these observations and the models is that the split between the model star forming and quiescent galaxies does not evolve as strongly as redshift increases (to higher star formation rates). This is in part because the center of quiescent branch, put in by hand, is currently fixed at all redshifts, while observationally the quiescent branch increases in star formation rate with redshift. (The model star forming branch does rise, although not fast enough for its peak to remain within the star forming branch of Moustakas et al (2013) at high redshift.)

For stellar mass functions, no variant matched observations perfectly for all redshifts, although the best fit to stellar mass functions at low redshift was based on a simulation with cosmology and mass definition similar to that used to construct the model's star formation efficiencies. Using a simulation based upon the current best fit cosmology

gives stellar mass functions which are too high at low redshift, consistent with the halo mass function being larger in the current best fit cosmology. At low redshift, using the instantaneous mass as dark matter halo mass rather than the smoothed and constrained $SAM_{M_{\text{vir}}}$ produced a slight increase in the stellar mass functions at the lower stellar masses, and using both instantaneous mass and only subtracting the mass of the most massive progenitor (rather than a weighted sum of all progenitor masses) gives a further increase. At high redshift, the stellar mass functions seem less sensitive to choices of halo mass and methods of inheriting stellar mass from progenitors. Some dependence upon cosmology remains. All tend to be high relative to the central value for the observed stellar mass functions, especially near the bend in the stellar mass function, although the models based upon the cosmology used to calculate the star formation efficiencies might be argued to be closer.

Dividing the quiescent and star forming galaxies according to the bimodality seen in star formation rate, the quiescent galaxy stellar mass function tended to be too high for all models at low stellar mass. For the tree model, where satellite subhalos are assigned their infall mass aside from mergers, satellites are almost all quiescent (about 1 percent have enough random star formation to be classified as star forming using the 'by eye' separation from the $M^* - SFR$ diagrams). The excess of faint quiescent galaxies also appears in the other models, however, which can have 1/3 or more satellites which are forming stars.

The models had two variations for inheriting stellar mass, from either 1 or 2 progenitors. These two cases tend to bracket the observed stellar mass function at low redshift and high stellar mass. At higher redshift, they get closer to each other but also increase relative to the observed stellar mass function, with both eventually lying mostly above at $z \sim 2$. The models all seem to be above the central stellar mass to halo mass relations calculated from observations, although close enough to be within errors for most cases. Aside from the tree model, the stellar mass to halo mass relation changed significantly between the 1 and 2 progenitor variants at high stellar mass, with the latter rising far above observations.

These results suggest some ways to improve the model.

- Presumably the star formation efficiencies would work better for the current cosmology simulations if the efficiencies were calculated assuming the best current fit cosmology. This should help with the overshoot in estimated stellar mass for many redshifts, perhaps including the tendency to fall high at high redshift for all the models. In addition, more data is now available on stellar mass functions and star formation rates at these redshifts.
- Tying the star formation rate of satellites to subhalo mass gain for satellites is difficult in some halo finders, for instance those which fix the satellite subhalo mass to infall mass aside from mergers. Perhaps some other way of having the satellite star formation rate evolve would also work (for instance the decaying star formation rate in Lu et al (2014), or the delayed quenching of Wetzel, Tinker, Conroy & van den Bosch (2013)¹⁴).

¹³ I thank M. White for suggesting this test.

¹⁴ I thank P. Behroozi for mentioning this latter variant is being explored by other groups.

- The quiescent branch, put in by hand, likely should increase in star formation rate as the redshift increases.
- It seems a combination of inheriting from 1 and 2 progenitors (or maybe more) might succeed. This could perhaps depend upon the stellar mass and/or mass ratios of progenitors¹⁵. For instance, Moster, Naab & White (2013) note that for higher halo mass, more stellar mass comes in from mergers, so perhaps some sort of final halo mass dependence would also be appropriate. The stellar mass to halo mass relation often shows a strong sensitivity to 1 or 2 progenitors contributing stellar mass.
- The high values of $M^*(M_h)$ relative to observations, if not improved by changing the cosmology to the current best fit (the current best fit cosmology has more high mass halos than that used in the star formation efficiencies (Rodriguez-Puebla et al 2016)), may be improved by making more stellar mass go into the ICL, even from a single progenitor.

It would be also interesting if certain properties (e.g. the excess of faint quiescent galaxies at high redshift) could not be improved by only changing the small number of physical assumptions currently in the model. The underlying assumption is that galaxies self-regulate (e.g. as in Schaye et al (2010); Hopkins, Quataert & Murray (2011)) their growth, so that the influx of halo mass (and thus presumably baryons) combined with the mass dependence of star formation is enough to capture many of the properties of evolution.

Looking at the ensemble of galaxy histories, with fixed final stellar mass, all 6 Becker (2015) based models considered had average histories differing from the semi-analytical models. For low final stellar mass galaxies, all 6 had very similar average histories, as final stellar mass increase, these became distinct. For the highest final stellar mass studied, $M^* = 10^{11} M_\odot$, the average histories of the 2 progenitor bol and bolp models, where the inherited stellar mass of a galaxy is the sum of that of its two largest progenitors, follows the average history of galaxies for which $M^* = M^*(M_h)$ at every time step. Compared to the two semi-analytic models, there is often more scatter around the average histories for the models constructed here (except for the highest final stellar mass), and they require the same or more basis fluctuations to capture at least 90% of the variance. It would be interesting to see how other similar simple models, e.g., Wang et al (2007); Bouché et al (2010); Cattaneo et al (2011); Mutch, Croton & Poole (2013); Lilly et al (2013); Tacchella, Trenti & Carollo (2013); Birrer et al (2014); Lu et al (2014, 2015), compare in these ensemble properties as well.

Given the simplicity of this model, it seems interesting to pursue it further, as it appears that many of its predictions work reasonably well at redshifts above zero. It would be interesting to look in further detail at the simulated galaxy populations, for instance to see if starbursting galaxies appear automatically within the population and if so, if their number agrees with observations. The dark matter simulations also include galaxy positions and velocities, and the full cosmological cosmic web. When more high redshift observations with large volume become available, it would be interesting to compare the model with additional observations such as clustering a function of stellar mass,

star formation rate (once that is better understood in the model) and environmental properties. For instance, if conformity of central galaxies in halos is indeed tied to halo growth Hearin, Behroozi & van den Bosch (2016), see also Hahn et al (2009), this effect is built into this model, as are other properties tying stellar mass and star formation rate to halo growth. It would also be interesting to push the model to higher redshifts.

ACKNOWLEDGEMENTS

I thank M. White for numerous discussions and use of his simulated TreePM data set, and Phillip Harris for early calculations of galaxy history PCA's. I also thank M. Becker, P. Behroozi, L. Guzzo, J. Moustakas, A. Munoz, N. Padilla, M. van Daalen, and F. van den Bosch, for discussions, A. Gonzalez and C. Mancone for help with and explanations of EZGAL, and J. Moustakas for sharing the PRIMUS results using different stellar mass assumptions, which was very helpful in order to explore their effects, and M. Becker, M. van Daalen and M. White for extremely helpful suggestions on an earlier draft, and the referee for helpful suggestions as well. This work was performed in part at the Aspen Center for Physics which is supported by National Science Foundation grant PHY-1066293. I am also grateful to the ROE and the IAP for hospitality during this work, and to the ROE for the opportunity to present this work in a seminar and get very helpful feedback as a result. The TreePM simulation by M. White was run at NERSC, and many of the models presented here were run there as well. The Millennium Simulation databases used in this paper and the web application providing online access to them were constructed as part of the activities of the German Astrophysical Virtual Observatory (GAVO). The Bolshoi-Planck simulation was performed by Anatoly Klypin within the Bolshoi project of the University of California High-Performance AstroComputing Center (UC-HiPACC) and was run at the NASA Ames Research Center. JDC was supported in part by DOE.

APPENDIX A: HOW TO MAKE VALIDATION PLOTS WITH YOUR SIMULATED DATA SET

The tests shown above are available (for testing one mock catalogue) at <https://www.github.com/jdcphysics/validation/> (the code and data are in the code subdirectory vsuite).¹⁶ They consist of a python file, `valid_suite.py`, and then several data files, many of which were kindly made available by the people who made and analyzed the observations. Observational data sets are described above in §3.3 and Table 2.

To run the python codes, you also need to have matplotlib and numpy, which will be imported when you run the program. To produce the plots above in §3 for one simulated model the command is:

¹⁶ To test the stellar mass function of more than one mock, modify the number of calls to the routine `getsimstellar` in `plot4tog` and `plot4sep`.

¹⁵ I thank M. van Daalen for these suggestions.

runsuite(zcen, fname, hval, omm, slopeval, shiftval, boxside, delz, ramin, ramax, decmin, decmax)

Here are two examples:

- fixed time periodic box of side $256 h^{-1}$ Mpc, redshift 0.45, data file “inputfile.dat”, hubble constant 0.67, $\Omega_m = 0.31$, default split of Moustakas et al (2013), i.e. Eq. 7, between star forming and quiescent galaxies.
runsuite(0.45, “inputfile.dat”, 0.67, 0.31, 0, 0, 256, “perbox”)
- light cone, where one wants to look at a slice $0.43 \leq z \leq 0.47$, ra and dec both between ± 2 , otherwise same as above:
runsuite(0.45, “inputfile.dat”, 0.67, 0.31, 0, 0, -1, “lc”, 0.02, -2, 2, -2, 2)

It can be useful to start with **slopeval**, **shiftval** = 0, and then vary these by looking at the stellar mass-star formation rate diagram, until the solid line falls between the two regions of star formation.

Parameters in detail:

- **zcen**: central redshift
- **fname**: input file name, in quotation marks, i.e. “inputfile.dat”
- **hval**: hubble constant h
- **omm**: Ω_m
- **slopeval**: Adjustments to quiescent vs. star forming galaxy split of PRIMUS (Moustakas et al 2013), i.e. in Eq. 7

$$\log(SFR_{\min}) = -0.49 + (0.65 + \text{slopeval})(\log M^* - 10) + 1.07(z - 0.1) + \text{shiftval} \quad (\text{A1})$$

divides quiescent and star forming galaxies.

- **shiftval**: see above (**slopeval**)
- **boxside**: box side in h^{-1} Mpc for fixed time periodic box, any negative number for light cone
- **runname**: a string, for name of run, e.g. “bolshoi”
- **delz**: δz , i.e. for light cone, keep galaxies in range $z - \delta z$ to $z + \delta z$, ignored for fixed time box.
- **ramin**: RA minimum value for light cone, ignored for fixed time box.
- **ramax**: RA maximum value for light cone, ignored for fixed time box.
- **decmin**: DEC minimum value for light cone, ignored for fixed time box.
- **decmax**: DEC maximum value for light cone, ignored for fixed time box.

The input file is a list of galaxies in the simulation, in ASCII format. Each galaxy is a different row, and the order and units of the entries are:

$\log_{10} M^*[M_\odot]$, SFR ($M^*[M_\odot]/\text{yr}$), RA, DEC, zred, ifsat, $\log_{10} M_h[M_\odot]$

- RA and DEC are ignored for a fixed time box, zred is used to calculate $M^*(M_h)$.
- ifsat = 0 if a central, 1 if a sat
- M_h ideally is M_{vir} , units are M_\odot (no h)

Here is an example of part of an input file for a periodic box (ra and dec are both set to 1 since they are not used,

and the redshift is set to that of the box):

$$\begin{array}{cccccccc} 9.428e+00 & 7.236e-01 & 1. & 1. & 0.00 & 0 & 11.3704 \\ 1.024e+01 & 1.913e-01 & 1. & 1. & 0.00 & 1 & 11.8632 \\ 9.501e+00 & 7.360e-02 & 1. & 1. & 0.00 & 0 & 11.3944 \\ 1.069e+01 & 1.459e-01 & 1. & 1. & 0.00 & 1 & 12.2967 \\ 9.400e+00 & 1.365e-01 & 1. & 1. & 0.00 & 0 & 11.3559 \\ 9.514e+00 & 7.470e-02 & 1. & 1. & 0.00 & 0 & 11.3944 \\ 1.053e+01 & 1.760e-01 & 1. & 1. & 0.00 & 0 & 12.1996 \\ 9.620e+00 & 1.136e-01 & 1. & 1. & 0.00 & 1 & 11.5112 \end{array} \quad (\text{A2})$$

The observational data used for the stellar mass functions depends upon the redshift, for the stellar mass to halo mass relation the curves are from (Moster, Naab & White 2013; Behroozi, Wechsler & Conroy 2013a), and the stellar mass-star formation rate plots can be compared to Fig. 1 of Moustakas et al (2013), for example.

APPENDIX B: $M^*(M_H)$ FITS TO OBSERVATIONS

The observational relations for $M^*(M_h)$ found by Moster, Naab & White (2013) are tuned to the observations of Perez-Gonzalez et al (2008) (664 arcmin²) and Santini et al (2012) (33 arcmin²). Those by Behroozi, Wechsler & Conroy (2013a) have the observations of Perez-Gonzalez et al (2008) (664 arcmin²) and Moustakas et al (2013) (5.5 deg²) in the same region. Both sets of observational stellar masses are found using the Bruzual & Charlot (2003) stellar population synthesis models with a Chabrier IMF. The relation from Moster, Naab & White (2013) is

$$\frac{M^*}{M_h} = 2N / [(\frac{M_h}{M_1})^{-\beta} + (\frac{M_h}{M_1})^\gamma] \quad (\text{B1})$$

(with their equations 11,12,13,14)

$$\begin{array}{ll} \log M_1(z) &= 11.590 + 1.195(1 - a) \\ N(z) &= 0.0351 - 0.0247(1 - a) \\ \beta(z) &= 1.376 - 0.826(1 - a) \\ \gamma(z) &= 0.608 + 0.329(1 - a) \end{array} \quad (\text{B2})$$

the best fit parameters are in their Table 1. The 1- σ errors on coefficients for $\log M_1$, N , β , γ are (in order appearing above) are (0.236, 0.353, 0.0058, 0.0069, 0.153, 0.225, 0.059, 0.173). Here M is halo mass, M_{200c} , and M^* is stellar mass.

The Behroozi, Wechsler & Conroy (2013a) fit is of the form (their equation 3)

$$\begin{aligned} \log_{10} M^*(M_h) &= \log_{10}(\epsilon M_1) + f(\log_{10}(M_h/M_1)) - f(0) \\ f(x) &= -\log_{10}(10^{\alpha x} + 1) \\ &\quad + \delta \frac{(\log_{10}(1+e^x))^\gamma}{1+\exp(10^{-x})} \end{aligned} \quad (\text{B3})$$

with parameters (section 5 of their paper)

$$\begin{array}{ll} \nu &= e^{-4a^2} \\ \alpha &= -1.412 + 0.731(a - 1)\nu \\ \delta &= 3.508 + (2.608(a - 1) - 0.043 z)\nu \\ \gamma &= 0.316 + (1.319(a - 1) + 0.279 z)\nu \\ \log_{10} M_1 &= 11.514 + (-1.793(a - 1) - 0.251 z)\nu \\ \log_{10} \epsilon &= -1.777 + (-0.006(a - 1) - 0.000 z)\nu \\ &\quad - 0.119(a - 1) . \end{array} \quad (\text{B4})$$

Both stellar mass to halo mass relations are plotted for each stellar mass bin in Fig. 6, but errors are not shown.

REFERENCES

- Baldry, I. K., Glazebrook, K., Brinkmann, J., Ivezić, Z., Lupton, R. H., Nichol, R. C., Szalay, A. S., 2004, *ApJ*, 600, 681
- Baldry, I. K., Glazebrook, K., Driver, S. P., 2008, *MNRAS*, 388, 945
- Baldry, I. K., Driver, S. P., Loveday, J., et al, 2012, *MNRAS*, 421, 621
- Baugh, C.M., 2006, *Rept. Prog. Phys.*, 69, 3101,
- Becker, M., 2015, *arXiv:1507.03605*
- Behroozi, P., Wechsler, R., Wu, H-Y., 2013, *ApJ*, 762, 109
- Behroozi, Peter S., Wechsler, Risa H., Wu, Hao-Yi, Busha, Michael T., Klypin, Anatoly A., Primack, Joel R., 2013, *ApJ*, 763, 18, code at <http://www.peterbehroozi.com/code.html>,
- Behroozi, P.S., Wechsler, R.H., Conroy, C., 2013a, *ApJ*, 770, 57,
- Behroozi, P.S., Wechsler, R.H., Conroy, C., 2013b, *ApJL*, 762, 31
- Bell, E. F., McIntosh, D. H., Katz, N., Weinberg, M. D., 2003, *ApJ Supp.*, 149, 289
- Benson, A.J., 2010, *Phys. Rep.*, 495, 33
- Birrer, S., Lilly, S., Amar, A., Aranjape, A., Refregier, 2014, *ApJ*, 793, 12
- Blanton, M. R., & Roweis, S. 2007, *AJ*, 133, 734
- Blumenthal, G. R., Faber, S.M., Primack, J. R., Rees, M. J., 1984, *Nature*, 311, 517
- Borgani, S. , Kravtsov, A.R., 2012, *ARA & A*, 50, 353
- Bouché, N., Dekel, A., Genzel, R., Genel, S., Cresci, G., Foerster Schreiber, N. M., Shapiro, K. L., Davies, R. I., Tacconi, L., 2010, *ApJ*, 718, 1001
- Bruzual, G., Charlot, S., 2003, *MNRAS*, 344, 1000
- Calzetti, D., Armus, L., Bohlin, R. C., et al 2000, *ApJ*, 533, 682
- Cardelli, Jason A., Clayton, Geoffrey C., Mathis, John S., 1989, *ApJ*, 345, 245
- Cattaneo, A., Mamon, G. A., Warnick, K., Knebe, A., 2011, *A&A* 533, 5
- Charlot, S., & Fall, S. M. 2000, *ApJ*, 539, 718
- Cohn, J.D., van de Voort, F., 2015, *MNRAS*, 446, 3253
- Conroy, C., Gunn, J., White, M., 2009, *ApJ*, 699, 486
- Conroy, C., Wechsler, R.H., 2009, *ApJ*, 696, 620
- Conroy, C., White, M., Gunn, J., 2010, *ApJ*, 708, 58
- Conroy, C., Gunn, J., 2010, *ApJ*, 712, 833
- Cooray, A., Sheth, R., 2002, *Phys. Reps.*, 372, 1
- Davis M., Efstathiou G., Frenk C.S., White S.D.M., 1985, *ApJ*, 292, 371
- Diemand J., Kuhlen M., Madau P., 2006, *ApJ*, 649, 1
- Dominguez Sanchez, H. et al, 2011, *MNRAS*, 417, 900
- Guo, Q., White, S., Angulo, R. E., Henriques, B., Lemson, G., Boylan-Kolchin, M., Thomas, P., Short, C., 2013, *MNRAS*, 428, 1351
- Hahn, O., Porciani, C., Dekel, A., Carollo, C.M., 2009, *MNRAS*, 398, 1742
- Hearin, A.P., Behroozi, P.S., van den Bosch, F.C., 2016, *MNRAS*, 461, 2135
- Hearin, A.P., Zentner, A.R., van den Bosch, F.C., Campbell, D., Tollerud, E., 2016, *MNRAS*, 460, 2552
- Henriques, B. M. B., White, S. D. M., Thomas, P. A., Angulo, R., Guo, Q., Lemson, G., Springel, V., Overzier, R., 2015, *MNRAS*, 451, 2663
- Hopkins, P.F., Quataert, E., Murray, N., 2011, *MNRAS*, 417, 950
- Ilbert O., Salvato M., Le Floch E., et al, 2010, *ApJ*, 709, 644
- Ilbert, O., McCracken, H. J., Le Fevre, O., et al, 2013, *Astronomy and Astrophysics Supplement Series*, 556, A55
- Klypin, A., Trujillo-Gomez, S., Primack, J., *ApJ*, 740, 102 (2011). rockstar trees at <http://www.slac.stanford.edu/~behroozi/Bolshoi.Trees/>
- Klypin, A., Yepes, G., Gottlober, S., Prada, F., Hess, S., 2016, *MNRAS*, 457, 4340 rockstar trees at <http://yun.ucsc.edu/sims/Bolshoi.Planck/trees/index.html>
- Kriek, M., van Dokkum, P. G., Labbé, I., et al 2009, *ApJ*, 700, 221
- Lemson, G., and the Virgo consortium, 2006, *arXiv:astro-ph/0608019*
- Li, C., White, S. D. M., 2009, *MNRAS*, 398, 2177
- Lilly, S. J., Carollo, C. M., Pipino, A., Renzini, A., Peng, Y., 2013, *ApJ*, 772, 119
- Lu, Z., Mo, H. J., Lu, Y., Katz, N., Weinberg, M. D., van den Bosch, F. C., Yang, X., 2014, *MNRAS*, 439, 1294
- Lu, Z., Mo, H. J., Lu, Y., Katz, N., Weinberg, M. D., van den Bosch, F. C., Yang, X., 2015, *MNRAS*, 450, 1604
- Madau, P., Dickinson, M., *ARA&A*, 52, 415
- Mancone, C. L., Gonzalez, A.H., 2012, *PASP*, 124, 606,
- Maraston, C., 2005, *MNRAS*, 362, 799
- Marchesini, D., van Dokkum, P. G., Forster Schreiber, N. M., Franx, M., Labbé, I., Wuyts, S., 2009, *ApJ*, 701, 1765
- Marchesini, D., Whitaker, K. E., Brammer, G., et al, 2010, *ApJ*, 725, 1277
- Mo, H., van den Bosch, F., White, S., 2010, *Galaxy Formation and Evolution*, Cambridge University Press, Cambridge
- Moster, B.P., Naab, T., White, S.D.M., 2013, *MNRAS*, 428, 3121,
- Moster, B. P., Somerville, R. S., Newman, J. A., Rix, H.-W., 2011, *ApJ*, 731, 113
- Moutard, T., et al, 2016, *A & A*, 590, 102
- Moustakas, J., et al, 2013, *ApJ* 767,50,
- Mutch, S. J., Croton, D. J., Poole, G. B., 2013, *MNRAS*, 435, 2445
- Muzzin, A., et al, 2013, *ApJ*, 777, 18
- Neistein, E., Khochfar, S., Dalla Vecchia, C., Schaye, J., 2012, *MNRAS*, 421, 3579
- Pacifici, C., Kassín, S.A., Weiner, B., Charlot, S., Gardner, J.P., 2013, *ApJL*, 762, 15
- Pacifici, C., Kassín, S.A., Weiner, B.J., et al, 2016, *ApJ*, 832, 79
- Peacock, J.A., Smith, R.E., 2000, *MNRAS*, 318, 1144
- Perez-Gonzalez et al, 2008, *ApJ*, 675, 234,
- Planck Collaboration, Ade et al, 2014, *A&A*, 571, 16
- Rodriguez-Puebla, A., Behroozi, P., Primack, J., Klypin, A., Lee, C., Helling, D., 2016, <http://arxiv.org/abs/1602.04813> , rockstar trees at <http://yun.ucsc.edu/sims/Bolshoi.Planck/trees/index.html>
- Santini, P., et al, 2012, *A&A*, 538, 33
- Schaye, J., et al, 2010, *MNRAS*, 402, 1536

- Seljak, U., 2000, MNRAS, 318, 203
 Smith, R.E., 2012, MNRAS, 426, 531
 Speagle, J. S., Steinhardt, C. L., Capak, P. L., Silverman, J. D. 2014, ApJS, 214, 15
 Springel, V., et al, 2005, Nature, 435, 629
 Stark, C., White, M., Lee, K.G., Hennawi, J.F., 2015, MNRAS, 453, 311
 Straatman, C.M.S., et al, 2016, ApJS, 830, 51
 Tacchella, S., Trenti, M., Carollo, M., 2013, ApJ, 768, L37
 Tasca, L.A.M., et al, 2015, A&A, 581, 54
 Tomczak, A.R., et al, 2014, ApJ, 783, 85,
 Vale, A., Ostriker, J.P., 2006, MNRAS, 371, 1173
 van den Bosch, F.C., 2016, arXiv:1611.02657
 Wang, L., Li, C., Kauffmann, G., De Lucia, G., 2007, MNRAS, 377, 1419
 Wetzel, A.R., White, M., 2010, MNRAS, 403, 1072
 Wetzel, A.R., Tinker, J.L., Conroy, C., van den Bosch, F.C., 2013, MNRAS, 432, 336
 White, S.D.M., Rees, M.J., 1978, MNRAS, 183, 341
 White M., 2001, A&A, 367, 27
 White M., 2002, ApJS, 143, 241
 White, M., Cohn, J.D., Smit, R., 2010, MNRAS, 408, 1818
 Wong, A.W.C., Taylor, J.E., 2011, ApJ, 757, 102
 Yang, X., Mo, H.J., van den Bosch, F.C., 2003, MNRAS, 339, 1057